Symmetry-preserving discretization of Navier–Stokes equations on collocated unstructured grids

F.X. Trias [a,b], O. Lehmkuhl [a,c], A. Oliva [a,*,1], C.D. Pérez-Segarra [a], R.W.C.P. Verstappen [b]

[a] *Heat and Mass Transfer Technological Center, Technical University of Catalonia, ETSEIAT, c/ Colom 11, 08222 Terrassa, Spain*
[b] *Johann Bernoulli Institute for Mathematics and Computing Science, University of Groningen, P.O. Box 407, 9700 AK Groningen, The Netherlands*
[c] *Termo Fluids, S.L., c/ Magí Colet 8, 08204 Sabadell, Spain*

ARTICLE INFO

ABSTRACT

A fully-conservative discretization is presented in this paper. The same principles followed by Verstappen and Veldman (2003) [3] are generalized for unstructured meshes. Here, a collocated-mesh scheme is preferred over a staggered one due to its simpler form for such meshes. The basic idea behind this approach remains the same: mimicking the crucial symmetry properties of the underlying differential operators, *i.e.*, the convective operator is approximated by a skew-symmetric matrix and the diffusive operator by a symmetric, positive-definite matrix. A novel approach to eliminate the checkerboard spurious modes without introducing any non-physical dissipation is proposed. To do so, a fully-conservative regularization of the convective term is used. The supraconvergence of the method is numerically showed and the treatment of boundary conditions is discussed. Finally, the new discretization method is successfully tested for a buoyancy-driven turbulent flow in a differentially heated cavity.

1. Introduction

We consider the simulation of turbulent, incompressible flows of Newtonian fluids. Under these assumptions, the dimensionless governing equations in primitive variables are

$$\frac{\partial \boldsymbol{u}}{\partial t} + (\boldsymbol{u} \cdot \nabla)\boldsymbol{u} = \frac{1}{Re}\Delta \boldsymbol{u} - \nabla p, \tag{1a}$$

$$\nabla \cdot \boldsymbol{u} = 0, \tag{1b}$$

where Re is the dimensionless Reynolds number. The basic physical properties of the Navier–Stokes (NS) equations can be deduced from the symmetries of the differential operators (see [1], for instance). In a discrete sense, it suffices to retain such operator symmetries to preserve the analogous (invariant) properties of the continuous equations. It may be argued, especially if the method is going to be used on unstructured meshes, that accuracy may need to take precedence over the properties of the operators. However, in this work, we have adopted the same philosophy followed by Verstappen and Veldman [2,3]: symmetries of the convective and diffusive operators are critical to the dynamics of turbulence and must be preserved.

* Corresponding author.
E-mail addresses: xavi@cttc.upc.edu (F.X. Trias), oriol@cttc.upc.edu (O. Lehmkuhl), cttc@cttc.upc.edu (A. Oliva), segarra@cttc.upc.edu (C.D. Pérez-Segarra), R.W.C.P.Verstappen@rug.nl (R.W.C.P. Verstappen).
[1] Tel.: +34 93 739 81 92; fax: +34 93 739 81 01.

1.1. A short historical review

Reconciling accuracy and stability has always been a great challenge for numerical simulation of turbulence. Upwind-like schemes have been very popular because they are very stable: the convective term introduces artificial numerical dissipation that systematically damps kinetic energy. Central difference schemes do not add non-physical dissipation, however, they do not guarantee stability. In the latter case, kinetic energy may need to be damped explicitly. Nevertheless, in both cases, the artificial false dissipation interferes with the subtle balance between convection transport and diffusive dissipation. This usually affects the smallest scales of motion, the essence of turbulence [3]. One solution to guarantee stability is to construct numerical approximations of the convective term that preserve total kinetic energy.

The importance of conservative discretization methods was realized in the pioneering works by Arakawa [4] and Arakawa and Lamb [5]. They showed that, for hydrostatic systems, the conservation of both kinetic energy and enstrophy by convective schemes prevent systematic and unrealistic energy cascade towards high wavenumbers, a cause of non-linear instability. Morinishi et al. [6] reviewed existing conservative, second-order finite-difference schemes for structured meshes, and introduced a fourth-order conservative scheme. However, for non-uniform meshes the truncation error was not fourth-order, so they chose to sacrifice conservation for accuracy and developed a "nearly conservative" fourth-order scheme. Later, Vasilyev [7] generalized the numerical schemes of Morinishi et al. to non-uniform meshes using a mapping technique. However, their schemes do not simultaneously preserve momentum and kinetic energy: it depends on the form chosen for the convective term [7].

Verstappen and Veldman [2,3] proposed to exactly preserve the symmetry properties of the underlying differential operators. The convective operator is represented by a skew-symmetric matrix and the diffusive operator by a symmetric, positive-definite matrix. The authors showed that such conditions are enough to ensure stability. With regard to the accuracy, they recalled the paper by Manteuffel and White [8]. In this work, the authors emphasized that local truncation error is not decisive: given stability, a second-order local truncation error is a sufficient, but not a necessary, condition for a second-order global truncation error. Moreover, they proved that the second-order symmetry-preserving discretization proposed in [2,3] yields a second-order accurate solution although its local truncation error is indeed first-order on non-uniform meshes. Finally, a fourth-order symmetry-preserving scheme is obtained removing the leading terms of the discretization error by means of a Richardson extrapolation. On uniform grids, conservative schemes by Verstappen and Veldman [2,3] become identical to those proposed by Morinishi et al. [6].

The way for accurate DNS and LES simulations on more complicated domains was opened by Perot [9] and Zhang et al. [10]. They derived a conservative staggered mesh scheme for unstructured grids. Later, Mahesh et al. [11] developed both staggered and collocated conservative schemes for LES in complex domains. More recently, Hicken et al. [12], presented a fully-conservative method for staggered unstructured grids. They use 'shift' transformations to obtain staggered operators from easy-to-define collocated operators. Thus, their formulation intends to lead to a generalization of the works by Perot [9] and Verstappen and Veldman [3]. However, it has only been put in practice on orthogonal unstructured grids. The extension of the ideas of Hicken et al. [12] to general unstructured meshes seems unlikely due to the impossibility to construct proper 'shift' transformations on such grids [13]. For further information about conservative schemes on unstructured grids, the reader is referred to the review article by Perot [14]. To complete this section, it is worth mentioning other related methods: namely, the Keller box schemes [15,16] and the mimetic schemes or support operators methods by Shashkov and Steinberg [17] and Hyman and Shashkov [18,19]. Finally, discrete calculus methods proposed by Perot and Subramanian [20] can be viewed as a general methodology for developing numerical methods that capture physics well. In this sense, most of the above-described conservative methods can be derived as discrete calculus methods. We can conclude, that nowadays it is generally accepted that the quality of the results is not automatically improved by simply increasing the order of accuracy of the numerical scheme [21]. Instead, the numerical schemes should retain the symmetry properties of the continuous equations. Very recent works in this vein can be found in [22–30], for instance.

The rest of the paper is arranged as follows. In the next section, it is shown that retaining the symmetry properties of the underlying continuous operators leads to spatial discretizations that exactly conserve the total kinetic energy for inviscid flows. Here, a collocated-mesh formulation is preferred over a staggered one due to its simpler form. This is also presented in Section 2. Special emphasis is given to the well-known checkerboard problem (see also Appendix A and Appendix B) and the properties of the 'shift' linear operator that relates the cell-centered and the staggered auxiliary velocity fields. A novel approach, based on a fully-conservative regularization of the convective term, is proposed to mitigate the checkerboard spurious modes. Then, in Section 3 the discrete operators are constructed taking into account all the constraints imposed by the global properties derived in the previous section. Finally, the new discretization method is numerically tested: (i) a simple experiment is performed to show the supraconvergence for a Poisson problem in Section 4 and (ii) DNS results for a turbulent differentially heated cavity are presented to show the accuracy and robustness of the method in Section 5. Finally, relevant results are summarized and conclusions are given.

2. Symmetry-preserving discretization on collocated grids

In this section, a conservative finite-volume discretization of the incompressible NS equations (1) on general unstructured grids is presented. Despite the intrinsic errors due to the improper pressure gradient formulation [6,31,32], here a collocated-mesh scheme is preferred over a staggered one due to its simpler form for unstructured grids. In this case, both
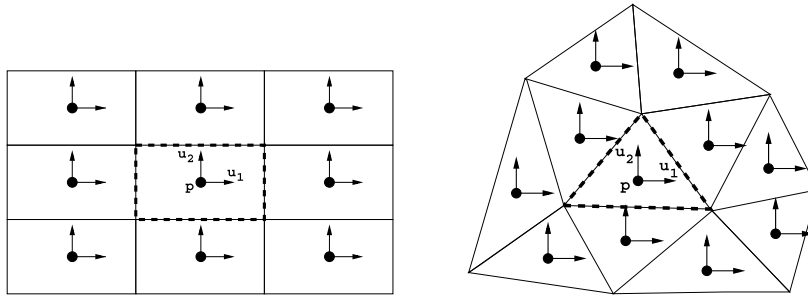
Fig. 1. Variable arrangement for a collocated-mesh scheme.

the pressure and the velocities are stored at the center of the control volume whereas a secondary velocity field is defined at the faces to enforce mass conservation in the control volumes (see Fig. 1). Special emphasis is given to the checkerboard problem and the properties of the face-to-center and center-to-face 'shift' operators. A novel approach, based on a fully-conservative regularization of the convective term, is proposed to mitigate the production of checkerboard spurious modes.

2.1. Definition of basic collocated operators

In a matrix–vector notation, the finite-volume discretization of the NS and continuity equations on an arbitrary collocated mesh can be written by

$$\Omega \frac{d\boldsymbol{u}_c}{dt} + C(\boldsymbol{u}_s)\boldsymbol{u}_c + D\boldsymbol{u}_c + \Omega G_c \boldsymbol{p}_c = \boldsymbol{0}_c, \tag{2a}$$

$$M\boldsymbol{u}_s = \boldsymbol{0}_c, \tag{2b}$$

where $\boldsymbol{p}_c = (p_1, p_2, \ldots, p_n)^* \in \mathbb{R}^n$ and $\boldsymbol{u}_c \in \mathbb{R}^{3n}$ are the cell-centered pressure and velocity fields and n is the number of control volumes. The subindices c and s refer to whether the variables are cell-centered or staggered at the faces. For simplicity $\boldsymbol{u}_c$ is defined as a column vector and arranged as $\boldsymbol{u}_c = (\boldsymbol{u}_1, \boldsymbol{u}_2, \boldsymbol{u}_3)^*$, where $\boldsymbol{u}_i = ((u_i)_1, (u_i)_2, \ldots, (u_i)_n)^*$ are the vectors containing the velocity components corresponding to the x_i-spatial direction. The auxiliary discrete staggered velocity field $\boldsymbol{u}_s = ((u_s)_1, (u_s)_2, (u_s)_3, \ldots, (u_s)_m)^* \in \mathbb{R}^m$ where m is the number of faces on the computational domain, is related with the centered velocity field via a linear shift transformation (interpolation) $\Gamma_{c \to s} \in \mathbb{R}^{m \times 3n}$,

$$\boldsymbol{u}_s \equiv \Gamma_{c \to s} \boldsymbol{u}_c. \tag{3}$$

The matrices $\Omega \in \mathbb{R}^{3n \times 3n}$, $C(\boldsymbol{u}_s) \in \mathbb{R}^{3n \times 3n}$ and $D \in \mathbb{R}^{3n \times 3n}$ are block diagonal matrices given by

$$\Omega = I_3 \otimes \Omega_c, \qquad C(\boldsymbol{u}_s) = I_3 \otimes C_c(\boldsymbol{u}_s), \qquad D = I_3 \otimes D_c, \tag{4}$$

where $I_3 \in \mathbb{R}^{3 \times 3}$ is the identity matrix and $\Omega_c \in \mathbb{R}^{n \times n}$ is a diagonal matrix with the cell-centered control volumes. $C_c(\boldsymbol{u}_s) \in \mathbb{R}^{n \times n}$ and $D_c \in \mathbb{R}^{n \times n}$ are the cell-centered convective and diffusive operators for a discrete scalar field, respectively. Note the $\boldsymbol{u}_s$-dependence of the convective operator (non-linear operator). Finally, $G_c \in \mathbb{R}^{3n \times n}$ represents the discrete gradient operator and the matrix $M \in \mathbb{R}^{n \times m}$ is the face-to-center discrete divergence operator.

2.2. (Skew-)symmetries of the collocated operators

The conservative nature of the NS equations is intimately tied up with the symmetries of the differential operators (see [1,3], for instance). In this section, it is shown that retaining such symmetries leads to spatial discretizations that exactly conserve the total kinetic energy for inviscid flows. In the forthcoming analysis we do not consider the effect of external sources (such as body and boundary forces). Therefore, we restrict ourselves to impervious or periodical boundary conditions. Following the same criterion than in [3], we define the discrete inner-product as follows

$$\langle \boldsymbol{v}_c, \boldsymbol{u}_c \rangle = \boldsymbol{v}_c^* \Omega \boldsymbol{u}_c, \tag{5}$$

then, the global discrete kinetic energy is given by $\|\boldsymbol{u}_c\|^2 \equiv \boldsymbol{u}_c^* \Omega \boldsymbol{u}_c$ and its temporal evolution equation can be obtained by left-multiplying Eq. (2a) by $\boldsymbol{u}_c^*$ and summing the resulting expression with its transpose

$$\frac{d}{dt}\|\boldsymbol{u}_c\|^2 = -\boldsymbol{u}_c^*\big(C(\boldsymbol{u}_s) + C^*(\boldsymbol{u}_s)\big)\boldsymbol{u}_c - \boldsymbol{u}_c^*\big(D + D^*\big)\boldsymbol{u}_c - \boldsymbol{u}_c^*\Omega G_c \boldsymbol{p}_c - \boldsymbol{p}_c^* G_c^* \Omega^* \boldsymbol{u}_c. \tag{6}$$

In absence of diffusion, that is $D = 0$, the global kinetic energy $\|\boldsymbol{u}_c\|^2$ is conserved if both, the convective and pressure terms, vanish (for any $\boldsymbol{u}_c$, $M\boldsymbol{u}_c = \boldsymbol{0}_c$) in the discrete kinetic energy equation,

$$\boldsymbol{u}_c^*\big(\mathsf{C}(\boldsymbol{u}_h)+\mathsf{C}^*(\boldsymbol{u}_h)\big)\boldsymbol{u}_c = 0, \tag{7a}$$

$$\boldsymbol{u}_c^*\Omega\mathsf{G}_c\boldsymbol{p}_c + \boldsymbol{p}_c^*\mathsf{G}_c^*\Omega^*\boldsymbol{u}_c = 0. \tag{7b}$$

The first equality is held if the discrete convective operator is skew-symmetric whereas defining the negative transpose of the discrete gradient operator to be exactly equal to the divergence operator, i.e.

$$\mathsf{C}(\boldsymbol{u}_s) = -\mathsf{C}^*(\boldsymbol{u}_s), \tag{8a}$$

$$-(\Omega\mathsf{G}_c)^* = \mathsf{M}\Gamma_{c\to s}, \tag{8b}$$

guarantees that the contribution of the pressure term also vanishes. Moreover, in this way the skew-symmetry of the continuous operators is preserved. Therefore, if the convective and gradient operators are properly chosen, the global kinetic energy equation reduces to

$$\frac{\mathrm{d}}{\mathrm{d}t}\|\boldsymbol{u}_c\|^2 = -\boldsymbol{u}_c^*(\mathsf{D}+\mathsf{D}^*)\boldsymbol{u}_c \leqslant 0, \tag{9}$$

where the inequality follows from the condition that the diffusive term must be strictly dissipative. Thus, the matrix $(\mathsf{D}+\mathsf{D}^*)$ must be positive-definite. Finally, although it is not strictly necessary [32], the diffusive operator, D, is assumed to be symmetric (and positive-definite) like the continuous operator, $-\Delta$. On the other hand, defining the total amount of momentum by taking the scalar product of the velocity vector, $\boldsymbol{u}_c$, with the vector $\Omega\mathbf{1}_c$, the equation for the temporal evolution of global momentum is obtained by left-multiplying Eq. (2a) by the vector $\mathbf{1}_c^*$

$$\frac{\mathrm{d}}{\mathrm{d}t}\big(\mathbf{1}_c^*\Omega\boldsymbol{u}_c\big) = -\mathbf{1}_c^*\big(\mathsf{C}(\boldsymbol{u}_s)+\mathsf{D}\big)\boldsymbol{u}_c - \mathbf{1}_c^*\Omega\mathsf{G}_c\boldsymbol{p}_c. \tag{10}$$

Therefore, momentum is conserved if $(\mathsf{C}(\boldsymbol{u}_s)+\mathsf{D})^*\mathbf{1}_c = \mathbf{0}_c$. Since the convective operator is skew-symmetric and the diffusive operator is symmetric we can leave the *'s away. Thus, it suffices to check that the constant vector $\mathbf{1}_c$ lies in the null space of both operators, i.e.

$$\mathsf{C}(\boldsymbol{u}_s)\mathbf{1}_c = \mathbf{0}_c \quad\text{and}\quad \mathsf{D}\mathbf{1}_c = \mathbf{0}_c. \tag{11}$$

2.3. Solving the pressure–velocity coupling. Checkerboard problem

In order to simplify the notation, spatially discrete momentum equation (2a) can be rewritten as follows

$$\frac{\mathrm{d}\boldsymbol{u}_c}{\mathrm{d}t} = \mathsf{R}(\boldsymbol{u}_c) - \mathsf{G}_c\boldsymbol{p}_c, \tag{12}$$

where $\mathsf{R}(\boldsymbol{u}_c) \equiv -\Omega^{-1}(\mathsf{C}(\boldsymbol{u}_s)\boldsymbol{u}_c + \mathsf{D}\boldsymbol{u}_c)$ represents the convective and diffusive terms. For the temporal discretization, a one-parameter fully explicit second-order one-leg scheme for $\mathsf{R}(\boldsymbol{u}_c)$ whereas the incompressibility constraint is treated implicitly. Then, the fully-discretized NS equations read

$$\mathsf{M}\boldsymbol{u}_s^{n+1} = \mathbf{0}_c, \tag{13a}$$

$$\frac{(\kappa+1/2)\boldsymbol{u}_c^{n+1} - 2\kappa\boldsymbol{u}_c^n + (\kappa-1/2)\boldsymbol{u}_c^{n-1}}{\Delta t} = \mathsf{R}\big((1+\kappa)\boldsymbol{u}_c^n - \kappa\boldsymbol{u}_c^{n-1}\big) - \mathsf{G}_c\boldsymbol{p}_c^{n+1}, \tag{13b}$$

where the parameter κ is computed each time-step to adapt the linear stability domain of the time-integration scheme to the instantaneous flow conditions in order to maximize the time-step, Δt [33]. To solve the velocity–pressure coupling, a classical fractional step projection method [34–36] is used. For the staggered velocity field, $\boldsymbol{u}_s$, this projection is 'naturally' derived from the Helmholtz–Hodge vector decomposition theorem [37], whereby a velocity $\boldsymbol{u}_s^p$ can be uniquely decomposed into a solenoidal vector, $\boldsymbol{u}_s^{n+1}$, and a curl-free vector, expressed as the gradient of a scalar field, $\mathsf{G}\tilde{\boldsymbol{p}}_c{}'$. This decomposition is written as

$$\boldsymbol{u}_s^p = \boldsymbol{u}_s^{n+1} + \mathsf{G}\tilde{\boldsymbol{p}}_c{}', \tag{14}$$

where $\mathsf{G} \in \mathbb{R}^{m\times n}$ is the center-to-face staggered gradient operator which is related with the divergence operator via

$$\mathsf{G} \equiv -\Omega_s^{-1}\mathsf{M}^*, \tag{15}$$

where $\Omega_s \in \mathbb{R}^{m\times m}$ is a diagonal matrix with the staggered control volumes. Then, taking the divergence of Eq. (14) yields a discrete Poisson equation for $\tilde{\boldsymbol{p}}_c{}'$

$$\mathsf{M}\boldsymbol{u}_s^p = \mathsf{M}\boldsymbol{u}_s^{n+1} + \mathsf{M}\mathsf{G}\tilde{\boldsymbol{p}}_c{}' \quad\longrightarrow\quad \mathsf{M}\mathsf{G}\tilde{\boldsymbol{p}}_c{}' = \mathsf{M}\boldsymbol{u}_s^p. \tag{16}$$

Finally, using the definition of G given in Eq. (15) the previous equation becomes

$$\mathsf{L}\tilde{\boldsymbol{p}}_c{'} = \mathsf{M}\boldsymbol{u}_s^p \quad \text{with } \mathsf{L} \equiv -\mathsf{M}\Omega_s^{-1}\mathsf{M}^*, \tag{17}$$

where the discrete Laplacian operator $\mathsf{L} \in \mathbb{R}^{n \times n}$ is, by construction, a symmetric negative-definite matrix. Notice that since the Laplacian operator inherits the boundary conditions from the divergence operator, no additional boundary conditions for pressure need to be prescribed. Once the solution is obtained, $\boldsymbol{u}_s^{n+1}$ results from the correction

$$\boldsymbol{u}_s^{n+1} = \boldsymbol{u}_s^p - \mathsf{G}\tilde{\boldsymbol{p}}_c{'}. \tag{18}$$

2.3.1. Constraints on the shift operators

However, on a collocated formulation the actual velocity is $\boldsymbol{u}_c$ and, therefore, the algorithm becomes necessarily more cumbersome. Firstly, linear shift operators are needed to relate the cell-centered velocity fields to the staggered ones and vice versa. Namely, the linear shift operator, $\Gamma_{c \to s} \in \mathbb{R}^{m \times 3n}$, transforms a cell-centered velocity field into a staggered one

$$\boldsymbol{u}_s = \Gamma_{c \to s}\boldsymbol{u}_c, \tag{19}$$

whereas the cell-centered fields are related to the staggered ones via the linear shift transformation $\Gamma_{s \to c} \in \mathbb{R}^{3n \times m}$,

$$\boldsymbol{u}_c = \Gamma_{s \to c}\boldsymbol{u}_s. \tag{20}$$

Notice, that in general $\Gamma_{s \to c}\Gamma_{c \to s} = \mathsf{I}$ holds only approximately *i.e.* $\boldsymbol{u}_c \approx \Gamma_{s \to c}\Gamma_{c \to s}\boldsymbol{u}_c$. More importantly, recalling the definition for the staggered gradient operator given in Eq. (15), the cell-centered discrete gradient operator results

$$\mathsf{G}_c = -\Gamma_{s \to c}\Omega_s^{-1}\mathsf{M}^*, \tag{21}$$

and, therefore, the face-to-cell shift operator $\Gamma_{s \to c}$ is restricted by Eq. (8b)

$$\left(\Omega\Gamma_{s \to c}\Omega_s^{-1}\mathsf{M}^*\right)^* = \mathsf{M}\Gamma_{c \to s} \quad \longrightarrow \quad \Gamma_{s \to c} = \Omega^{-1}\Gamma_{c \to s}^*\Omega_s, \tag{22}$$

to force that the pressure gradient contribution to the global kinetic energy exactly vanishes.

2.3.2. Computing the cell-center predictor velocity $\boldsymbol{u}_c^p$

In the projection method, the predicted velocity, $\boldsymbol{u}_c^p$, is computed as follows

$$\boldsymbol{u}_c^{p1} = \frac{2\kappa\boldsymbol{u}_c^n - (\kappa - 1/2)\boldsymbol{u}_c^{n-1}}{\kappa + 1/2} + \frac{\Delta t}{\kappa + 1/2}\mathsf{R}\bigl((1 + \kappa)\boldsymbol{u}_c^n - \kappa\boldsymbol{u}_c^{n-1}\bigr), \tag{23}$$

$$\boldsymbol{u}_c^p = \boldsymbol{u}_c^{p1} - \mathsf{G}_c\tilde{\boldsymbol{p}}_c{}^p, \tag{24}$$

where $\tilde{\boldsymbol{p}}_c{}^p$ is a 'prediction' of the pressure at the next time-step, $\tilde{\boldsymbol{p}}_c{}^{n+1} = \tilde{\boldsymbol{p}}_c{}^p + \tilde{\boldsymbol{p}}_c{'}$. Then, the discrete Poisson equation to be solved results

$$\mathsf{L}\tilde{\boldsymbol{p}}_c{'} = \mathsf{M}\boldsymbol{u}_s^p = \mathsf{M}\Gamma_{c \to s}\boldsymbol{u}_c^{p1} - \mathsf{M}\Gamma_{c \to s}\mathsf{G}_c\tilde{\boldsymbol{p}}_c{}^p. \tag{25}$$

In a staggered formulation, the definition of $\tilde{\boldsymbol{p}}_c{}^p$ is irrelevant from the point-of-view of the numerical solution [38]. This is not the case for the collocated counterpart. Actually, an additional error term proportional to the third-order derivative of $\tilde{\boldsymbol{p}}_c{'}$ is implicitly added to the momentum equation. This goes in the same vein as the approach proposed by Rhie and Chow [39] and, therefore, it suffices for eliminating the checkerboard modes in the pressure field [40,41]. This issue is addressed in Appendix A where two limiting situations are analyzed: (i) $\tilde{\boldsymbol{p}}_c{}^p = \boldsymbol{0}_c$ and (ii) $\tilde{\boldsymbol{p}}_c{}^p = \tilde{\boldsymbol{p}}_c{}^n$. The former is the classical Chorin projection [34] whereas the later corresponds to the second-order van Kan projection method [42]. Hereafter, these two approaches will be referred as total pressure (TP) and pressure correction (PC), respectively. It is shown that this additional term leads to an unphysical contribution to kinetic energy that scales like (i) $\mathcal{O}(\Delta t^2)$ and (ii) $\mathcal{O}(\Delta t^4)$, respectively. For details the reader is referred to Appendix A.

2.3.3. Correction of the cell-center predictor velocity $\boldsymbol{u}_c^p$. Origin of the checkerboard problem

Cell-center predictor velocity field, $\boldsymbol{u}_c^p$, is computed from Eqs. (23) and (24) and then corrected to obtained the velocity field at the next time-step, $\boldsymbol{u}_c^{n+1}$. The overall correction algorithm can be explicitly written by combining the expressions (19), (18), (17) and (20) and forcing that $\boldsymbol{u}_c^p \approx \Gamma_{s \to c}\Gamma_{c \to s}\boldsymbol{u}_c^p$ is exactly satisfied, *i.e.*

$$\boldsymbol{u}_c^{n+1} = \boldsymbol{u}_c^p + \Gamma_{s \to c}\Omega_s^{-1}\mathsf{M}^*\mathsf{L}^{-1}\mathsf{M}\Gamma_{c \to s}\boldsymbol{u}_c^p. \tag{26}$$

Then, introducing the definition of the face-to-cell operator (22) we obtain

$$\boldsymbol{u}_c^{n+1} = \boldsymbol{u}_c^p + \Omega^{-1}\Gamma_{c \to s}^*\mathsf{M}^*\mathsf{L}^{-1}\mathsf{M}\Gamma_{c \to s}\boldsymbol{u}_c^p = \bigl(\mathsf{I} - \Omega^{-1}\mathsf{P}\bigr)\boldsymbol{u}_c^p \quad \text{with } \mathsf{P} = -\Gamma_{c \to s}^*\mathsf{M}^*\mathsf{L}^{-1}\mathsf{M}\Gamma_{c \to s}, \tag{27}$$

where the matrix $P \in \mathbb{R}^{3n \times 3n}$ is, by construction, symmetric and positive-definite. Notice that the discrete Laplacian operator, L, given in Eq. (17) is symmetric and negative-definite. At this point, it must be noted that the matrix $(I - \Omega^{-1}P)$ is not exactly a projector, i.e. $(I - \Omega^{-1}P)^2 \approx (I - \Omega^{-1}P)$, unless $\Gamma_{c \to s}\Gamma_{s \to c} = I$. At this stage, special care must be taken in order to avoid unphysical velocity components in the numerical solution. The so-called checkerboard problem is related with the unrealistic components of the cell center velocity field that the pseudo-projection matrix cannot eliminate,

$$\boldsymbol{u}_c^{\ominus} = \left(I - \Omega^{-1}P\right)\boldsymbol{u}_c^{\ominus}, \tag{28}$$

where $\boldsymbol{u}_c^{\ominus}$ represents these spurious modes (see the velocity field decomposition defined in Eq. (B.1)). This implies that $\boldsymbol{u}_c^{\ominus}$ lies on the kernel of P,

$$\boldsymbol{u}_c^{\ominus} \in Ker(P). \tag{29}$$

Hence, these 'unrealistic' velocity components cannot be corrected unless they are explicitly removed. However, to do so, we need to accurately determine $Ker(P)$. In general, this is not feasible for real-world applications except for simple mesh topologies where the kernel is known a priori [25]. In the following subsection we try to elucidate the origin of such 'unrealistic' velocity components as well the possible ways to keep our numerical solution free from these unphysical oscillations. See also Appendix B for further details.

2.4. Symmetry-preserving regularization of the convective term. Stopping the production of spurious modes

Since the convective term is the source of the unphysical spurious modes (see Appendix B), a modification of this term is needed. Here, we consider regularizations [43,44] (smooth approximations) of the non-linearity. The idea behind regularization methods is to alter the convective term in order to restrain the production of small scales of motion. Mathematically, they reduce the dynamical complexity of the original NS equations and the resulting governing equations are more amenable to be numerically solved. Hence, from this perspective, regularizations can be viewed as a turbulence model. The first outstanding approach in this direction goes back to Leray [45]. In this case, the convective term is replaced by

$$C_{Leray}(\boldsymbol{u}_s, \boldsymbol{v}_c) \equiv C(\overline{\boldsymbol{u}_s})\boldsymbol{v}_c, \tag{30}$$

where the $\overline{(\cdot)}$ represents a discrete linear filter. Many examples of Leray regularization being used as a turbulence model can be found in the literature (see [46–48], for instance). However, regularizations can also be viewed as an alternative form of discretization. As a preview of things, we consider the discretization of the convective term in one spatial dimension. Let us consider three values of a smooth function $u(x)$: $u_{i-1} = u(x_{i-1})$, $u_i = u(x_i)$ and $u_{i+1} = u(x_{i+1})$ with $x_{i-1} = x_i - h$ and $x_{i+1} = x_i + h$. By a simple combination of Taylor-series expansions of $u(x)$ around $x = x_i$, the following second-order accurate approximation follows

$$u(x_i)\partial_x u(x_i) \approx u_i \frac{u_{i+1} - u_{i-1}}{2h}, \tag{31}$$

whereas a Leray regularization can be easily obtained by simply considering the classical three-point filter, $\overline{u}_i = 1/4(u_{i-1} + 2u_i + u_{i+1})$,

$$\overline{u(x_i)}\partial_x u(x_i) \approx \overline{u}_i \frac{u_{i+1} - u_{i-1}}{2h} = \frac{1}{4}(u_{i-1} + 2u_i + u_{i+1})\frac{u_{i+1} - u_{i-1}}{2h}. \tag{32}$$

This filter is obtained by applying the trapezoidal rule to compute the average of the variable, u, over $x_{i-1} \leqslant x \leqslant x_{i+1}$. The same formula may also be derived by simply discretizing the convective term in divergence form

$$\frac{1}{2}\partial_x u^2(x_i) \approx \frac{1}{2}\frac{u_{i+1/2}^2 - u_{i-1/2}^2}{h} \approx \frac{1}{2}\frac{(\frac{u_{i+1}+u_i}{2})^2 - (\frac{u_i+u_{i-1}}{2})^2}{h} = \frac{1}{4}(u_{i-1} + 2u_i + u_{i+1})\frac{u_{i+1} - u_{i-1}}{2h}, \tag{33}$$

and considering a midpoint formula to approximate the variable, u, at $i + 1/2$ and $i - 1/2$, respectively. Thus, the same expression can be used to approximate both $\overline{u(x_i)}\partial_x u(x_i)$ and $1/2\partial_x u^2(x_i) = u(x_i)\partial_x u(x_i)$. Hence, regularizations can also be viewed as an alternative form of deriving discretizations of the convective term. At this stage, in order to be coherent with the previous analysis, the symmetry and conservation properties of the convective terms must be exactly preserved too. This is not the case of Leray regularization [49]. Alternatively, we propose to use the C_4 approximation proposed by Verstappen [49]: the convective term is then replaced by the following $\mathcal{O}(\epsilon^4)$-accurate smooth approximation given by

$$C_4(\boldsymbol{u}_s, \boldsymbol{v}_c) \equiv C(\overline{\boldsymbol{u}_s})\overline{\boldsymbol{v}_c} + \overline{C(\overline{\boldsymbol{u}_s})\boldsymbol{v}_c'} + \overline{C(\boldsymbol{u}_s')\overline{\boldsymbol{v}_c}}, \tag{34}$$

where the prime indicates the residual of the filter, e.g. $\boldsymbol{u}_c' = \boldsymbol{u}_c - \overline{\boldsymbol{u}_c}$, which can be explicitly evaluated, and $\overline{(\cdot)}$ represents a linear filter, $\overline{\boldsymbol{u}_c} = G_\epsilon \boldsymbol{u}_c$, with filter length ϵ. The fourth-order accuracy respect to ϵ follows straightforwardly from the observation that $\boldsymbol{u}_c' = \mathcal{O}(\epsilon^2)\boldsymbol{u}_c$ [50]. In order to preserve the symmetry and conservation properties of the convective operator, a normalized self-adjoint filter is needed

$$\mathsf{G}_\epsilon \mathbf{1}_c = \mathbf{1}_c, \tag{35a}$$

$$(\Omega_c \mathsf{G}_\epsilon) = (\Omega_c \mathsf{G}_\epsilon)^* \quad \Longrightarrow \quad (\mathsf{G}_\epsilon \boldsymbol{u}_c)^* \Omega_c \boldsymbol{v}_c = \boldsymbol{u}_c \Omega_c (\mathsf{G}_\epsilon \boldsymbol{v}_c). \tag{35b}$$

Note that the C_4-approximation is also a skew-symmetric operator, $\mathsf{C}_4 = -\mathsf{C}_4^*$, like the original convective operator. Hence, the same inviscid invariants—kinetic energy, enstrophy in 2D and helicity—than the original NS equations are preserved for the new set of equations. For a detailed mathematical analysis the reader is referred to [49] where the C_4-regularization was originally proposed as a new turbulence modeling approach. However, as state above, if the filter length, ϵ, is taken proportional to the mesh step-size, h, then C_4 can also be viewed as an $\mathcal{O}(h^4)$-accurate approximation of C. Therefore, the leading term of the global truncation error of the convective term is not being affected when the C_4 approximation is being used instead of C. Doing so, the convective term becomes smooth enough to mitigate the production of checkerboard spurious modes without introducing any non-physical dissipation. The reader is referred to Appendix B.2 for details.

3. Constructing the discrete operators

The discretization of the operators preserving the global properties is addressed in this section. In general, the constraints imposed by the operator (skew-)symmetries strongly restrict the form of the local approximations limiting, in some cases, the local truncation error.

3.1. Reynolds transport theorem

To prepare for the finite-volume symmetry-preserving discretization, we recall the Reynolds transport theorem for a smooth function ϕ

$$\frac{\mathrm{d}}{\mathrm{d}t} \int_{(\Omega_c)_{k,k}} \phi \, \mathrm{d}V = \int_{(\Omega_c)_{k,k}} \frac{\partial \phi}{\partial t} \, \mathrm{d}V + \int_{\partial(\Omega_c)_{k,k}} \phi \boldsymbol{u} \cdot \boldsymbol{n} \, \mathrm{d}S, \tag{36}$$

on an arbitrary centered cell k of volume $(\Omega_c)_{k,k}$. Note that, the function ϕ can have several physical meanings depending on what is being transported.

3.2. Collocated convective operator

Second term of the right-hand side of Eq. (36) can be exactly expressed as

$$\int_{\partial(\Omega_c)_{k,k}} \phi \boldsymbol{u} \cdot \boldsymbol{n} \, \mathrm{d}S = \sum_{f \in F_f(k)} \int_{S_f} \phi \boldsymbol{u} \cdot \boldsymbol{n} \, \mathrm{d}S, \tag{37}$$

where $F_f(k)$ is the set of faces bordering the cell k. Assuming that the discrete normal velocities, $[\boldsymbol{u}_s]_f \approx \boldsymbol{u}_f \cdot \boldsymbol{n}_f$, are located at the centroid of the face, then a second-order discretization of the integral (37) is given by

$$\int_{\partial(\Omega_c)_{k,k}} \phi \boldsymbol{u} \cdot \boldsymbol{n} \, \mathrm{d}S \approx \sum_{f \in F_f(k)} \phi_f [\boldsymbol{u}_s]_f A_f, \tag{38}$$

where A_f is the area of the face f. Hence, the collocated convective operator is defined by its action on an arbitrary cell-centered scalar field $\boldsymbol{\phi}_c \in \mathbb{R}^n$ at some cell k as

$$\big[\mathsf{C}_c(\boldsymbol{u}_s)\boldsymbol{\phi}_c\big]_k = \sum_{f \in F_f(k)} \phi_f [\boldsymbol{u}_s]_f A_f. \tag{39}$$

3.2.1. Skew-symmetry of the convective operator

In Section 2.2, we have seen that the convective contribution to the global kinetic energy vanishes if the convective operator is skew-symmetric (Eq. (8a)). Such a condition is easily verified in two steps [3]. Firstly, we consider the off-diagonal elements. The matrix $\mathsf{C}_c(\boldsymbol{u}_s) - \mathrm{diag}(\mathsf{C}_c(\boldsymbol{u}_s))$ is skew-symmetric if the interpolation weights of the adjacent discrete variables are taken equal to $1/2$, hence independent of their spatial coordinates

$$\phi_f \approx [\Pi_{c \to s} \boldsymbol{\phi}_c]_f = \frac{\phi_{c1} + \phi_{c2}}{2}, \tag{40}$$

where $c1$ and $c2$ are the cells adjacent to the face f (see Fig. 2, left) and $\Pi_{c \to s} \in \mathbb{R}^{m \times n}$ is the shift operator that interpolates a cell-centered scalar field to the faces. Then, for the skew-symmetry of the collocated convective operator, $\mathsf{C}_c(\boldsymbol{u}_s)$, the diagonal elements must be zero

$$\big[\mathsf{C}_c(\boldsymbol{u}_s)\big]_{k,k} = \frac{1}{2} \sum_{f \in F_f(k)} [\boldsymbol{u}_s]_f A_f = 0. \tag{41}$$
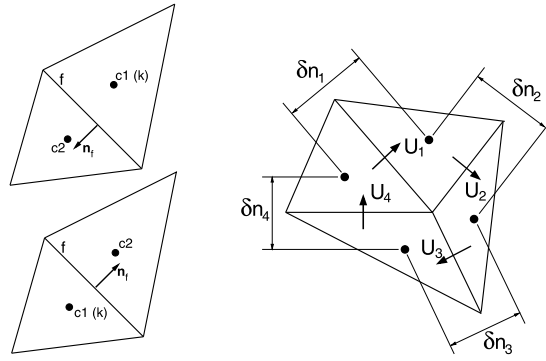
Fig. 2. Left: face normal and neighbor labeling criteria. Right: definition of the volumes of the face-normal velocity cell.

In conclusion, the collocated convective operator $C_c(\boldsymbol{u}_s)$ is skew-symmetric if the discrete centered variable ϕ is interpolated to the faces of the control volumes using the rule defined in Eq. (40), and Eq. (41) is accomplished. In the following section, we will see that the latter condition holds if the divergence operator, M, is consistently defined.

3.3. Gradient, divergence and Laplacian operators

Integrating the continuity equation (1b) over an arbitrary centered cell k of volume $(\Omega_c)_{k,k}$ yields

$$\int\limits_{(\Omega_c)_{k,k}} \nabla \cdot \boldsymbol{u}\, \mathrm{d}V = \int\limits_{\partial(\Omega_c)_{k,k}} \boldsymbol{u} \cdot \boldsymbol{n}\, \mathrm{d}S = \sum_{f \in F_f(k)} \int\limits_{S_f} \boldsymbol{u} \cdot \boldsymbol{n}\, \mathrm{d}S. \tag{42}$$

Note that taking ϕ equal to the unity, the Reynolds transport theorem (36) also gives the continuity equation in integral form. Therefore, Eq. (38) is particularized to define the proper integrated divergence operator,

$$[\mathsf{M}\boldsymbol{u}_s]_k = \sum_{f \in F_f(k)} [\boldsymbol{u}_s]_f A_f = 0. \tag{43}$$

Doing so, we are forcing the diagonal elements of the collocated convective operator to be equal to zero (see Eq. (41)). At this stage, it must be noted that the collocated convective operator defined in Eq. (39) can be rewritten by using more basic operators as follows

$$C_c(\boldsymbol{u}_s)\boldsymbol{\phi}_c = \mathsf{M}\big(\mathrm{diag}(\Pi_{c \to s}\boldsymbol{\phi}_c)\boldsymbol{u}_s\big). \tag{44}$$

In Section 2.2, we have defined (see Eq. (15)) the integrated pressure gradient operator, $\Omega_s\mathsf{G}$, to be equal to the negative transpose of the divergence operator, $-\mathsf{M}^*$. Hence, the discretization of the pressure gradient at the face f follows from Eq. (43),

$$[\Omega_s\mathsf{G}\boldsymbol{p}_c]_f = (p_{c1} - p_{c2})A_f, \tag{45}$$

where $c1$ and $c2$ are the cells adjacent to the face f (see Fig. 2, left). The order of accuracy of the discretization of the gradient operator defined in Eq. (45) is, in general, $\mathcal{O}(1)$. Since for incompressible flows, the role of the pressure gradient is to project the velocity field into a divergence-free space, this lack of accuracy becomes irrelevant in this context. Also note that since the discrete gradient inherits the boundary conditions from the discrete divergence operator, we need not to specify the boundary conditions for the pressure. Finally, we compute the pressure from a Poisson equation, which arises from the incompressibility constraint. The Laplacian operator is approximated by the matrix,

$$\mathsf{L} = -\mathsf{M}\Omega_s^{-1}\mathsf{M}^*, \tag{46}$$

which is symmetric and negative-definite, like the continuous Laplacian operator, $\Delta \equiv \nabla \cdot \nabla$.

3.4. Diffusive operator

Again, a diffusive operator is easily constructed on a collocated mesh. The same method for discretization the Laplacian operator is also applied. The diffusive operator is viewed as the product of two first-derivative-based operators: the divergence, M, of a gradient, G,

$$\mathsf{D}_c = -\frac{1}{Re}\mathsf{M}\mathsf{G} = \frac{1}{Re}\mathsf{M}\Omega_s^{-1}\mathsf{M}^*. \tag{47}$$

The Reynolds number has been introduced in order to simplify the forthcoming notation. Note that the collocated diffusive operator is, by definition (see Eq. (47)), symmetric and positive-definite and its action on a cell-centered variable is given by,

$$[D_c \phi_c]_k = \frac{1}{Re} \sum_{f \in F_f(k)} \frac{(\phi_{c2} - \phi_{c1})A_f}{\delta n_f},$$ (48)

where the length δn_f is an approximation of the distance between the centroids of the cells $c1$ and $c2$ given by $\delta n_f = |\mathbf{n}_f \cdot \overline{c1c2}|$. Then, the volume of the face-normal velocity cell at the face f is defined as $(\Omega_s)_f = \delta n_f A_f$ (see Fig. 2, right). Notice that on general unstructured meshes (Ω_s) is not a partition of unity, $\mathrm{tr}(\Omega_s) \neq \mathrm{tr}(\Omega_c)$, and the local truncation error of the diffusive discretization is indeed $\mathcal{O}(1)$. Therefore, at first sight this operator definition might seem inappropriate. However, supraconvergence for the global truncation error has been observed in numerical experiments (see Section 4, for details).

3.5. Shift operators

The linear shift transformation, $\Gamma_{c \to s} \in \mathbb{R}^{m \times 3n}$, is given by

$$[\Gamma_{c \to s} \mathbf{u}_c]_f = \left[N_s(\Pi \mathbf{u}_c) \right]_f = \frac{1}{2} \left([\mathbf{u}_c]_{c1} + [\mathbf{u}_c]_{c2} \right) \cdot \mathbf{n}_f,$$ (49)

where matrices $N_s \in \mathbb{R}^{m \times 3m}$ and $\Pi \in \mathbb{R}^{3m \times 3n}$ are respectively given by

$$N_s = \left(N_{s,1} \quad N_{s,2} \quad N_{s,3} \right) \quad \text{and} \quad \Pi = I_3 \otimes \Pi_{c \to s},$$ (50)

where $N_{s,i} \in \mathbb{R}^{m \times m}$ are diagonal matrices containing the x_i-spatial components of the face normal vectors, and $\Pi_{c \to s} \in \mathbb{R}^{m \times n}$ is the operator that interpolates a cell-centered scalar field to the faces defined in Eq. (40). Finally, face-to-cell shift transformation, $\Gamma_{s \to c} \in \mathbb{R}^{3n \times m}$, follows straightforwardly from Eq. (22).

3.6. Choice of the linear filter

A linear filter, $G_\epsilon \in \mathbb{R}^{3n \times 3n}$, is needed to compute the C_4 approximation of the convective term defined in Eq. (34). The properties specified in Eqs. (35) must be held in order to preserve the symmetry and conservation properties of the convective operator. Many types of filters can be found in the literature [51]; however, in general, their implementation on unstructured grids can be cumbersome. Instead, we adopted the criterion that filters should be based on already available operators and fulfill the properties given in Eqs. (35) by construction. In this way, they can be straightforwardly implemented on any mesh. This point has been recently addressed in [52] where a new family of discrete linear filters was proposed. To sketch the idea behind, linear filters are based on polynomial functions of the discrete diffusive operator,

$$G_\epsilon = I + \sum_{m=1}^{\mathcal{M}} d_m \tilde{D}^m \quad \text{with } \tilde{D} = -Re\,\Omega^{-1}D,$$ (51)

where the boundary conditions that supplement the NS equations (1a) are applied in (51) too. Notice that the factor Re cancels out the diffusive constant inside the operator D defined in Eqs. (4) and (47). Here we restrict ourselves to the case with $\mathcal{M} = 2$ because it offers a good compromise between accuracy and computational cost (see [52], for details). Following the same notation than in [52], the resulting expression for the filter with $\mathcal{M} = 2$ is given by

$$d_1 = -\frac{\widehat{G}_{k_c} - 1}{2(2\widehat{G}_{k_c} + 1)} \qquad d_2 = \frac{2\widehat{G}_{k_c}^2 - 3\widehat{G}_{k_c} + 1}{16(2\widehat{G}_{k_c} + 1)} \quad \text{if } 0 \leqslant \widehat{G}_{k_c} < 1/2,$$

$$d_1 = \frac{1}{4} - \frac{\widehat{G}_{k_c}}{4} \qquad d_2 = 0 \quad \text{if } 1/2 \leqslant \widehat{G}_{k_c} \leqslant 1,$$ (52)

where $\widehat{G}_{k_c}$ is the value of transfer function at the smallest grid scale. Then, recalling that $\mathbf{u}' = -(\epsilon^2/24)\Delta \mathbf{u}$ (see [51], for instance), the filter length, ϵ can be easily related with $\widehat{G}_{k_c}$ via

$$\widehat{G}_{k_c} \approx \frac{12 - \epsilon^2}{12 + 2\epsilon^2}.$$ (53)

Hence, $\epsilon = 2$ leads to $\widehat{G}_{k_c} = 0.4$; and $\epsilon = 3$ leads to $\widehat{G}_{k_c} = 0.1$. Numerical tests presented in Section 5 were carried out for both values. Although the differences were minimal, we observed that the performance of the method with $\widehat{G}_{k_c} = 0.1$ was slightly better. Therefore, for the remainder of the paper we consider $\widehat{G}_{k_c} = 0.1$.
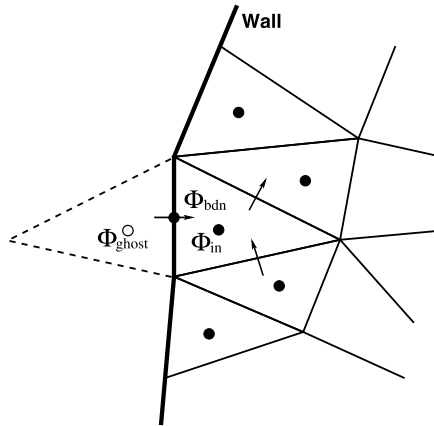
Fig. 3. Boundary conditions treatment.

3.7. Boundary conditions

Since now we have not considered the numerical treatment of the boundary conditions. Obviously, symmetry properties have to be preserved for those cases with no contribution from the boundaries, *e.g.* periodic or no-slip boundary conditions. In the case of periodic boundary conditions, their discretization can be easily extended without breaking the symmetries of the matrices C and D. For non-periodic boundary conditions it is not so clear. The operators have to be discretized in such a way that their symmetry properties are preserved.

3.7.1. Boundary conditions for the convective operator

The discretization near the boundary is not constructed to minimize the local truncation error. Instead, we have to take care to build it without violating the skew-symmetry of the matrix C. The collocated convective operator at the cell ϕ_{in} (see Fig. 3, left) is defined according to the expressions (39) and (40). To do so, we need to evaluate the out-of-domain variable ϕ_{ghost}. Firstly, we consider that such *ghost* variable only depends on ϕ_{in} and the boundary value ϕ_{bdn}, *i.e.*

$$\phi_{ghost} = f^{C}(\phi_{bdn}, \phi_{in}). \tag{54}$$

Therefore, the off-diagonal coefficients remain unchanged. Then, we have to construct a linear extrapolation function f^{C} in such a way that the skew-symmetry of C is exactly preserved,

$$\phi_{ghost} = a_{bdn}\phi_{bdn} + a_{in}\phi_{in}, \tag{55}$$

then, the diagonal element becomes

$$\left[C_c(\boldsymbol{u}_s)\right]_{k,k} = \frac{1}{2}\sum_{f \in F_f(k)} [\boldsymbol{u}_s]_f A_f - \frac{1}{2}\left([\boldsymbol{u}_s]_f A_f\right)_{bdn}(1 + a_{in}). \tag{56}$$

Thus, it would remain null, if and only if, the coefficient a_{in} is taken equal to -1. Finally, imposing that the interpolated face variable at the boundary be equal to ϕ_{bdn} yields

$$\phi_{ghost} = 2\phi_{bdn} - \phi_{in}. \tag{57}$$

3.7.2. Diffusive operator

The coefficient matrix D_c is defined as $Re^{-1} M\Omega_s^{-1}M^*$ (see Eq. (47)) where the matrix Ω_s^{-1} is a positive diagonal matrix. Hence, symmetry and positive-definiteness occurs naturally also at the boundaries. Notice that the condition (57) is implicitly imposed when constructing the divergence operator M.

4. Supraconvergence

The accuracy of a numerical method has been traditionally analyzed in terms of its local truncation error. However, Manteuffel and White [8] showed that the local truncation error only provides a lower bound for the global truncation error. In practice, it is possible that low-order terms cancel providing a better real accuracy. This is the case for symmetry-preserving discretizations on structured Cartesian grids [3,12]. In the context of finite-volume (finite-difference also) schemes this behavior is called supraconvergence (see [53] and references therein).
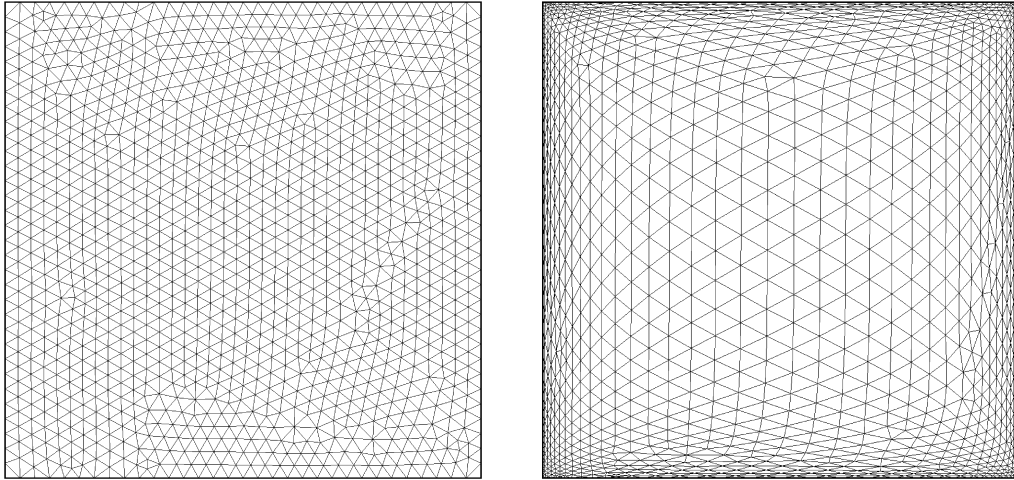
Fig. 4. Left: one of the unstructured 2D grids with triangular elements used to solve the problem given in Eq. (58). Right: the same mesh but stretched to the boundaries using the mapping function (59) with $\gamma = 2$.

However, for unstructured grids the analytical analysis becomes more difficult and tedious. A second type of errors appears due to the misalignments between the faces and cells centers. Hicken et al. [12] only provides evidence that the order of accuracy is not affected by these errors. However, their analysis is only restricted for an unstructured Cartesian method that benefits from the symmetry of the refinements. Thus, general unstructured meshes may have larger convergence errors. A complete analytical approach for the general case is beyond the scope of this paper. Instead, the following problem

$$\Delta\varphi = f \quad \text{on } \Omega = (0,1) \times (0,1) \quad \text{and} \quad \varphi|_{\partial\Omega} = 0, \tag{58}$$

with $f(x_1, x_2) = \Delta(A^{-2} \sin(Ax_1) \sin(Ax_2))$ and $A = 25\pi$ has been numerically solved on 150 different meshes using the discrete approximation of the Laplacian operator defined in Eq. (46). The ANSYS ICEM CFD package has been used to randomly generate unstructured 2D grids with triangular elements (see Fig. 4, right). In Fig. 5 (top), the norm of the error, $\|R_h\varphi - \varphi_h\|_\infty$, and the norm of the local truncation error, $\|R_h f - \mathsf{L} R_h \varphi\|_\infty$, are plotted versus the average step-size defined as $\mathrm{tr}(\Omega_c)/n$, where $R_h \in \mathbb{R}^{n \times n}$ is the operator that define point-wise restrictions on the mesh nodes. For convenience, different scales have been used. The straight lines are the least-squares fit to the points and have slopes 0.62 and 1.94, respectively.

The same test has also been carried out for more anisotropic grids. In this case, the meshes have been generated by mapping the previous ones with the following hyperbolic-tangent function,

$$x_2^{map} = \frac{1}{2}\left(1 + \frac{\tanh\{\gamma(2x_2 - 1)\}}{\tanh\gamma}\right), \tag{59}$$

for both spatial directions to stretch them to the walls. An example thereof is displayed in Fig. 4 (right) where a concentration factor of $\gamma = 2$ has been applied. The results obtained for this value of γ are displayed in Fig. 5 (bottom). For this case, the rates of convergence of the local and the global truncation errors are $p_{loc} = 0.26$ and $p_{glob} = 2.45$, respectively. In Table 1, the results obtained for other concentration factors are also shown. As expected, the rate of convergence of the local truncation error, p_{loc}, tends to degrade for more anisotropic meshes. More importantly, for all the tests performed the rate of convergence of the global truncation error is always around (or higher than) 2.

These examples only provide evidence of the supraconvergence of the discrete Laplacian operator, L. Moreover, since the diffusive operator is nothing more than three Laplacian operators (see Eqs. (4), (47) and (46)), a similar behavior must be expected for D. Regarding the convective operator, $\mathsf{C}(\boldsymbol{u}_s)$, its local truncation error is indeed $\mathcal{O}(h^a)$, with $1 \leqslant a \leqslant 2$ depending on the quality of the local grid refinements. Therefore, its global truncation errors must possess, at least, the same order of accuracy.

At this point, it must be noted that the matrix $\mathsf{C}(\boldsymbol{u}_s) + \mathsf{D}$ is regular, because all the eigenvalues lie in the stable half-plane. This is important for the relationship between the global and the local truncation errors. For instance, in the stationary case, the global truncation error is equal to the product of the inverse of $\mathsf{C}(\boldsymbol{u}_s) + \mathsf{D}$ and the local truncation error. Therefore, a (nearly) singular discrete operator can destroy the favorable properties of the local truncation error. Examples of this behavior for non-symmetry-preserving discretizations can be found in [54].

5. Test-case: turbulent differentially heated cavity

In this section the performance of the symmetry-preserving discretization presented in this work is assessed through application to a 2D buoyancy-driven turbulent flow in an air-filled ($Pr = 0.71$) differentially heated cavity (see Fig. 6, left).
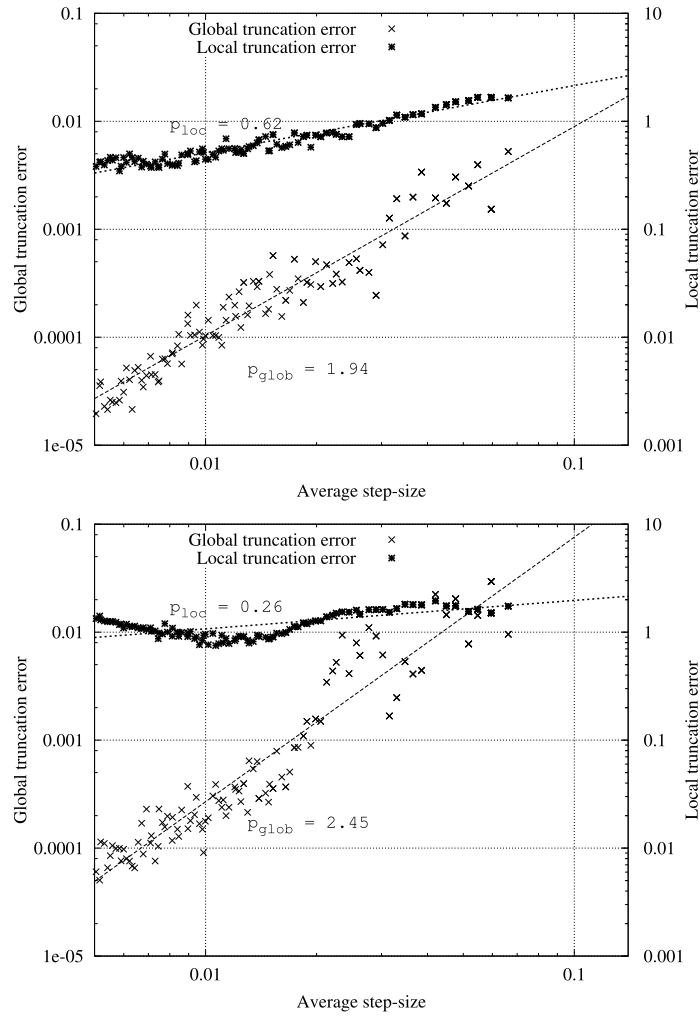
Fig. 5. The norm of the global truncation error, $\|R_h\varphi - \varphi_h\|_\infty$, and the norm of the local truncation error, $\|R_h f - LR_h\varphi\|_\infty$, versus the average step-size, $\mathrm{tr}(\Omega_c)/n$, for the problem defined in Eq. (58). Results are plotted in a log–log scale. They correspond to mesh concentration factors $\gamma = 0$ (top) and $\gamma = 2$ (bottom), respectively.

Table 1
Rates of convergence of the local and the global truncation errors for the problem defined in Eq. (58) for different values of the mesh concentration factor, γ.

γ	0.0	0.5	1.0	1.5	2.0
p_{loc}	0.62	0.52	0.29	0.24	0.26
p_{glob}	1.94	1.98	2.05	2.28	2.45

This configuration has been chosen because it can be discretized with both structured Cartesian and unstructured meshes. The cavity is subjected to a temperature difference, $\Delta T = T_H - T_C$, across the vertical isothermal walls while the top and bottom horizontal walls are adiabatic. The no-slip boundary condition is imposed on the velocity field. For this case, the reference length, time, velocity and temperature are respectively L_3, $(L_3^2/\alpha)Ra^{-0.5}$, $(\alpha/L_3)Ra^{0.5}$ and ΔT, where α is the thermal diffusivity. In Fig. 6 (right), several instantaneous temperature maps corresponding to the DNS at Rayleigh number $Ra = 10^{10}$ (based on the cavity height, L_3) and height aspect ratio $L_3/L_2 = 4$ are displayed. They illustrate the inherent flow complexity of this configuration: namely, the vertical boundary layers remain laminar in their upstream part up to the point where the waves traveling downstream grow up enough to disrupt the boundary layers ejecting large unsteady eddies. The mixing effect of these eddies results into almost isothermal hot upper and cold lower regions, and forces the temperature drop in the core of the cavity to occur in a smaller region. Turbulent fluctuations are only significant in the downstream part of the boundary layers for x_3-locations downstream the transition point (see Fig. 6, right). Therefore, an accurate prediction of the flow structure in the cavity lies on the ability to locate the transition to turbulence correctly. However, the high sensitivity of the thermal boundary layer to external disturbances makes it difficult to predict (see [55], for instance).

Fig. 6. Differentially heated cavity problem. Left: general schema. Right: Several instantaneous temperature fields at $Ra = 10^{10}$. General view of the cavity and a time sequence of three instantaneous isotherms. Zoom around the top left corner. Dimensionless time-step between consecutive snapshots is ≈ 0.281.

Therefore, this is a challenging test-case for a spatial discretization. Since the formulation is collocated, the additional temperature transport equation has been discretized in the same way. The DNS results were presented in [56] and the reader is referred to that work for further details. In that case, the simulation was carried out on a structured Cartesian staggered mesh using a fourth-order symmetry-preserving discretization [3]. Since we used the same time-integration method [33], the differences can only be attributed to the spatial discretization itself. Hereafter, those results will be referred as StgDNS and will be used as a reference solution. For the sake of comparison, we keep the same notation and coordinate system than in [56].

5.1. Structured Cartesian collocated mesh

Firstly, the collocated symmetry-preserving discretization has been tested for a structured Cartesian mesh. This allows to analyse the effect of using the collocated formulation itself. Moreover, on such grids the kernel of the pseudo-projector P defined in Eq. (27) is known *a priori*. Namely, for a 2D mesh it is spanned by the modes

$$Ker(\mathsf{P}) = \left\{ \begin{array}{c} \boldsymbol{\phi}_c^u \\ \boldsymbol{\phi}_c^v \end{array} \right\} \quad \text{with } u, v = 0, 1, 2, 3, \tag{60}$$

where the cell-center scalar fields $\boldsymbol{\phi}_c^u \in \mathbb{R}^n$ and $\boldsymbol{\phi}_c^v \in \mathbb{R}^n$ are given by

$$\left[\boldsymbol{\phi}_c^0\right]_{ij} = 1, \qquad \left[\boldsymbol{\phi}_c^1\right]_{ij} = (-1)^i, \qquad \left[\boldsymbol{\phi}_c^2\right]_{ij} = (-1)^j, \qquad \left[\boldsymbol{\phi}_c^3\right]_{ij} = (-1)^{i+j}. \tag{61}$$

Hence, for this particular case $\dim(Ker(\mathsf{P})) = 16 \ (= 4^2)$. Those modes containing the constant scalar field, $\boldsymbol{\phi}_c^0$, can be discarded from the analysis because they are not compatible with the prescribed boundary conditions. Therefore, from a practical point-of-view we can consider that the dimension of the kernel reduces to $9 \ (= 3^2)$. The extension of this analysis for 3D is straightforward. In that case, the kernel of P also includes odd–even oscillations in the x_1-direction and the corresponding velocity component; therefore, its dimension is $343 \ (= 7^3)$.

The computational domain is covered by a Cartesian mesh with the faces of the control volumes distributed using a hyperbolic-tangent function

$$(x_i)_k = \frac{1}{2} \frac{L_i}{L_3} \left(1 + \frac{\tanh\{\gamma_i(2(k-1)/N_i - 1)\}}{\tanh \gamma_i} \right), \quad k = 1, \ldots, N_i + 1. \tag{62}$$

The spatial resolution in these two directions was determined by means of a systematic procedure based on successive mesh refinements (see [56], for details). The mesh concentration factors, γ_2 and γ_3, were computed to minimize the flow gradients on the computational space for a set of representative instantaneous maps. The region most sensitive to the grid resolution is near the vertical isothermal wall. The grids considered in this analysis are listed in Table 2. For the two finest meshes the first grid point is located in wall units at $x_2^+ \lesssim 0.45$ (MeshA) and $x_2^+ \lesssim 0.63$ (MeshB), respectively (see Table 2). Note that the friction velocity, u_τ, is computed from the local wall-shear stress. In [56], it was shown that the MeshB suffices to obtain an accurate solution. Therefore, for the sake of lower computational costs the MeshA has not been considered in the first preliminary studies where two important issues have been addressed. Namely, the effect of the pressure gradient treatment and the control of the checkerboard spurious modes.

Fig. 7 displays the time evolution of the normalized contributions to the total kinetic energy for different meshes and numerical treatments of the pressure correction. The time-averaged values of these results are shown in Table 3. They

Table 2
Physical and numerical simulation parameters for the structured Cartesian meshes.

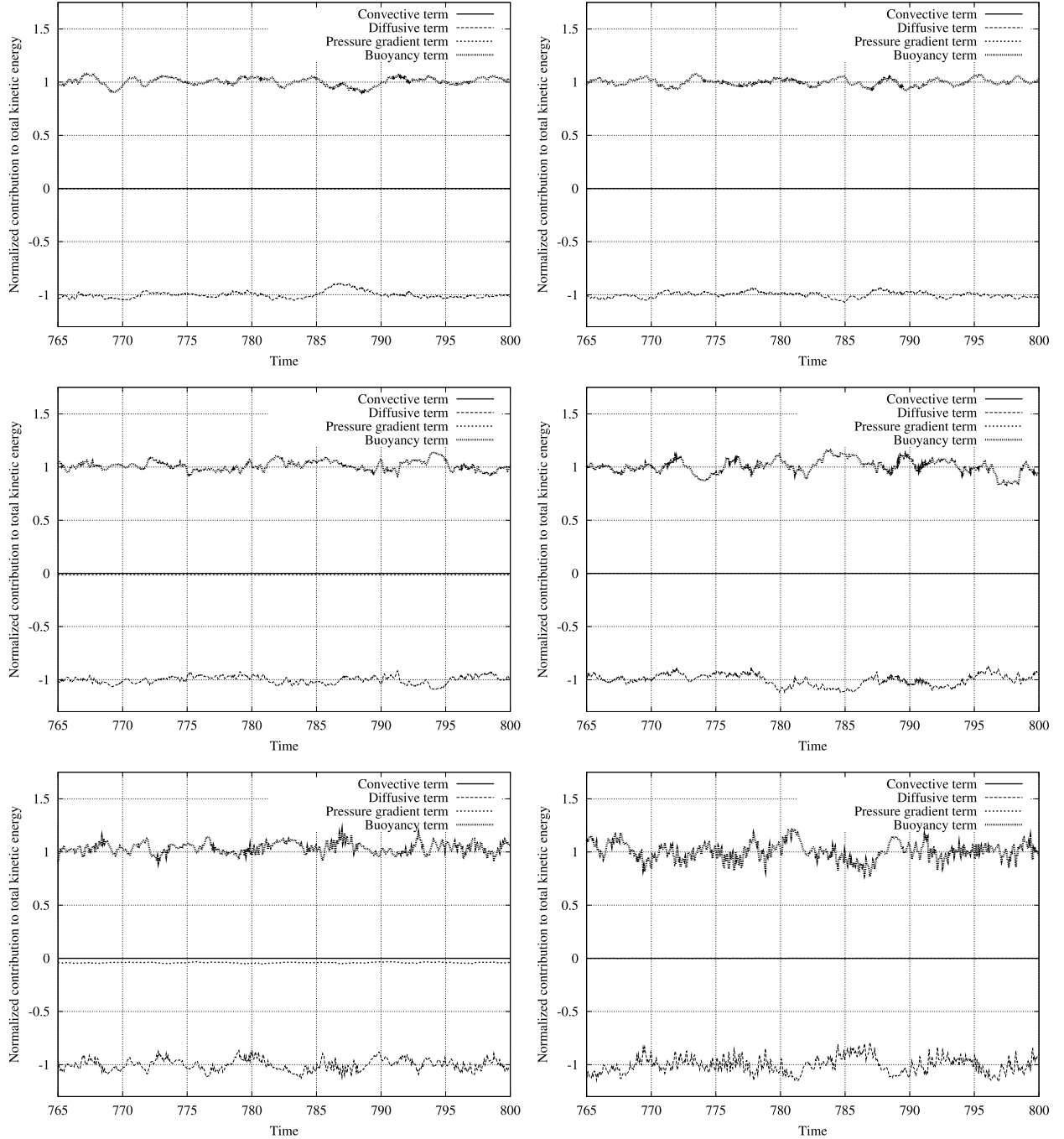| Case	N_2	N_3	γ_2	γ_3	$(\Delta x_2)_{min}$	$(\Delta x_2)^+_{min}$	Δt	Total time	Average time	Order
StgDNS	194	459	2.0	0.0	9.63×10^{-5}	$\lesssim 0.45$	7.56×10^{-4}	256	175	4
MeshA	194	460	2.0	0.0	9.63×10^{-5}	$\lesssim 0.45$	7.55×10^{-4}	800	400	2
MeshB	138	326	2.0	0.0	1.35×10^{-4}	$\lesssim 0.63$	1.39×10^{-3}	800	400	2
MeshC	98	230	2.0	0.0	1.91×10^{-4}	$\lesssim 0.89$	2.64×10^{-3}	800	400	2
MeshD	72	166	2.0	0.0	1.91×10^{-4}	$\lesssim 1.21$	4.64×10^{-3}	800	400	2

Fig. 7. Time evolution of the normalized contributions to the total kinetic energy for different meshes (from top to bottom: MeshB, MeshC and MeshD) and numerical treatments of the pressure correction (left: total pressure; right: pressure correction). A summary of these results is shown in Table 3.

Table 3
Time-averaged normalized contributions to the total kinetic energy for different meshes and numerical treatments of the pressure correction. TP and PC stand for the total pressure and pressure correction approaches, respectively.

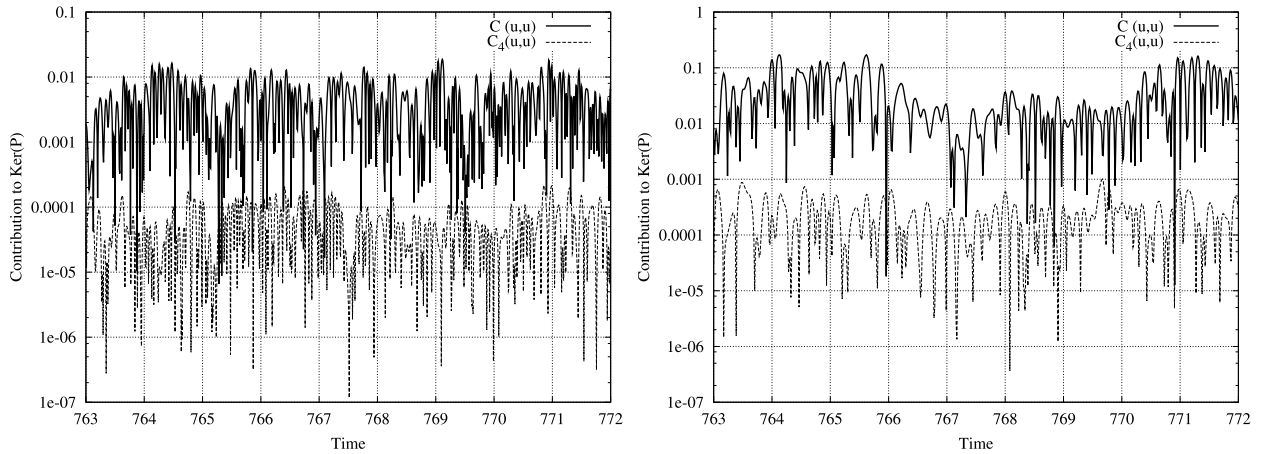| TP/PC	Mesh	Conv	Diff	Buoyancy	PressGrad	Δt	Order
TP	MeshB	≈ 0	-1	1.0047	-3.65×10^{-3}	1.39×10^{-3}	
	MeshC	≈ 0	-1	1.0119	-1.23×10^{-2}	2.64×10^{-3}	1.95
	MeshD	≈ 0	-1	1.0394	-4.16×10^{-2}	4.64×10^{-3}	
PC	MeshB	≈ 0	-1	1.0009	-3.24×10^{-6}	1.39×10^{-3}	
	MeshC	≈ 0	-1	1.0035	-5.08×10^{-5}	2.64×10^{-3}	3.73
	MeshD	≈ 0	-1	0.9988	-2.92×10^{-4}	4.64×10^{-3}	

Fig. 8. Time evolution of the total contribution of the convective term to $Ker(\mathsf{P})$ for MeshC (left) and MeshD (right).

correspond to the statistically steady state and are normalized respect to the averaged total dissipation rate. As expected, in all the cases the total contribution of the convective term is zero (except round-off errors). Then, the dynamical system should be governed by a balance between buoyancy terms (production) and physical dissipation (destruction). However, the pressure gradient term can interfere this balance. As expected, this non-physical contribution is significantly lower for the pressure correction procedure. Even more important, the measured order of convergence respect to the time-step, Δt, is also higher (see Table 3): namely, 1.95 for the total pressure (TP) approach and 3.73 for the pressure correction (PC) approach. These results are in good agreement with the expected orders of convergence (see Appendix A). Another important feature of the method is that this unphysical contribution remains negative; therefore, it guarantees the stability of the method (see Appendix B, for details).

Regarding the control of the checkerboard spurious modes, the straightforward approach (without regularization) and the C_4-regularization approach have been compared. Given a velocity vector field, $\boldsymbol{u}_c$, a natural approach to measure its spurious modes is the L^2-norm

$$\|\boldsymbol{u}_c\|_\ominus^2 = \|\boldsymbol{u}_c^\ominus\|^2 = (\boldsymbol{u}_c^\ominus)^* \Omega \boldsymbol{u}_c^\ominus \quad \text{with } \boldsymbol{u}_c^\ominus = P_{Ker(\mathsf{P})}\boldsymbol{u}_c, \tag{63}$$

where $P_{Ker(\mathsf{P})} \in \mathbb{R}^{2n \times 2n}$ is the projection onto the $Ker(\mathsf{P})$ given in Eq. (60). Fig. 8 displays both $\|\Omega^{-1}\mathsf{C}(\boldsymbol{u}_s)\boldsymbol{u}_c\|_\ominus^2$ and $\|\Omega^{-1}\mathsf{C}_4(\boldsymbol{u}_s, \boldsymbol{u}_c)\|_\ominus^2$ corresponding to the statistically steady state for MeshC (left) and MeshD (right). Since the level of production of spurious modes increases for coarser grids we only show the results obtained for the two coarsest meshes. For both cases the results are essentially the same: the proposed C_4-regularization approach keeps the total contribution to the $Ker(\mathsf{P})$ around two orders of magnitude lower that the straightforward implementation. These results confirm the adequacy of the method to significantly mitigate the amount of unphysical spurious modes in the numerical solution without introducing any non-physical damping effect.

Finally, the results obtained for the collocated formulation are compared with the StgDNS results. A summary of several time-averaged statistics is presented in Table 4. Namely, the overall averaged Nusselt number, $Nu = \int_0^1 Nu(x_3) \, dx_3$ where $Nu(x_3) = -\partial \langle T \rangle / \partial x_2|_{x_2=0}$ is the Nusselt number distribution at the hot wall and $\langle \cdot \rangle$ represents the average over time. The transition point at the vertical boundary layer, x_3^{Tr}, is defined as the x_3-position of the $\sigma(Nu(x_3))_{\max}$ where $\sigma(\cdot)$ denotes the standard deviation. Regarding the boundary layer, three additional results are also shown: the maximum averaged vertical velocity at the horizontal mid-plane and its x_2-position together with the averaged wall-shear stress at the mid-cavity height. As expected all these quantities are in good agreement with the reference solution for both MeshA and MeshB. The results obtained with the two coarsest meshes are far from the reference solution simply because the mesh is not fine enough. Nevertheless, since the method is unconditionally stable numerical solutions are obtained even for very

Table 4
Summary of averaged results for the structured Cartesian grids defined in Table 2. By rows, from top to bottom, the magnitudes are: the overall averaged Nusselt number, the minimum of the averaged local Nusselt, the transition point at the vertical boundary layer, the maximum of $\langle u_3 \rangle$ at the horizontal mid-plane and its x_2-position, the averaged wall-shear stress at the mid-cavity height, the dimensionless stratification in the core of the cavity, the frequency corresponding to the peak of the spectrum of the Nusselt number through the vertical mid-plane and the Brunt–Väisälä frequency.

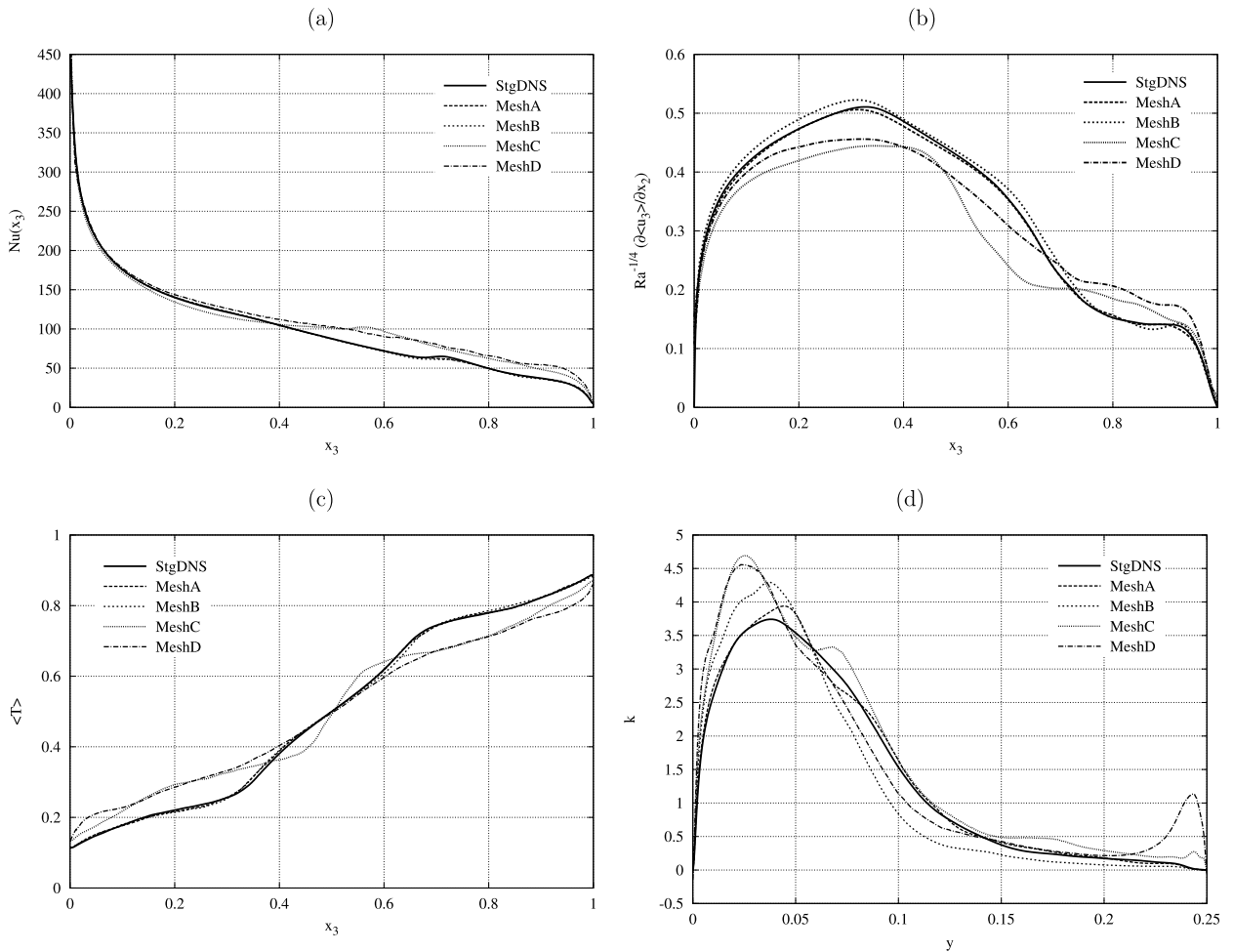|	StgDNS	MeshA	MeshB	MeshC	MeshD
Nu	100.6	100.5	100.5	107.0	111.2
$Nu(x_3)_{min}$	5.1	5.2	5.6	8.5	11.0
x_3^{Tr}	0.712	0.738	0.729	0.552	0.02
$(\langle u_3 \rangle\|_{x_3=0.5})_{max}$	0.223	0.228	0.227	0.203	0.196
x_2 $(\times 10^3)$	3.75	3.75	3.75	4.50	4.50
$Ra^{-1/4}\frac{\partial \langle u_3 \rangle}{\partial x_2}\|_{x_2=0, x_3=0.5}$	0.430	0.426	0.436	0.370	0.387
C	1.08	1.05	1.01	2.06	0.909
f_{Nu_c}	0.152	0.132	0.134	0.186	0.150
N	0.140	0.137	0.135	0.193	0.128

(a)

(b)

(c)

(d)

Fig. 9. Time-averaged results for the structured Cartesian grids defined in Table 2. (a) The local Nusselt number distribution, $Nu(x_3)$ at the hot wall. (b) The averaged wall-shear stress scaled by $Ra^{-1/4}$ at the hot wall. (c) The averaged temperature vertical profile at mid-width cavity. (d) Horizontal profile at $x_3 = 0.8$ of the turbulent kinetic energy, k.

coarse meshes. Regarding the structure of the cavity core, the dimensionless stratification, $C = \partial \langle T \rangle / \partial x_3|_{\{x_2=0.5L_2/L_3, x_3=0.5\}}$, is shown in Table 4 too. Again, this value is rather well predicted for the two finest meshes. Finally, regarding the flow dynamics, the frequency, f_{Nu_c}, corresponding to the peak of the spectrum of the Nusselt number through the vertical mid-plane, $Nu_c(t) = \int_0^1 (u_2 T - \partial T / \partial x_2)|_{x_2=0.5L_2/L_3} \, dx_3$ and the Brunt–Väisälä frequency, $N = (C \, Pr)^{0.5}/(2\pi)$ are also listed in Table 4. Since these fundamental frequencies are related with the internal wave motion of the thermally stratified cavity core, a good agreement with the StgDNS results is only achieved when the thermal stratification is correctly predicted too. The same conclusions can be obtained from the plots displayed in Fig. 9: the flow structure is only well predicted for the
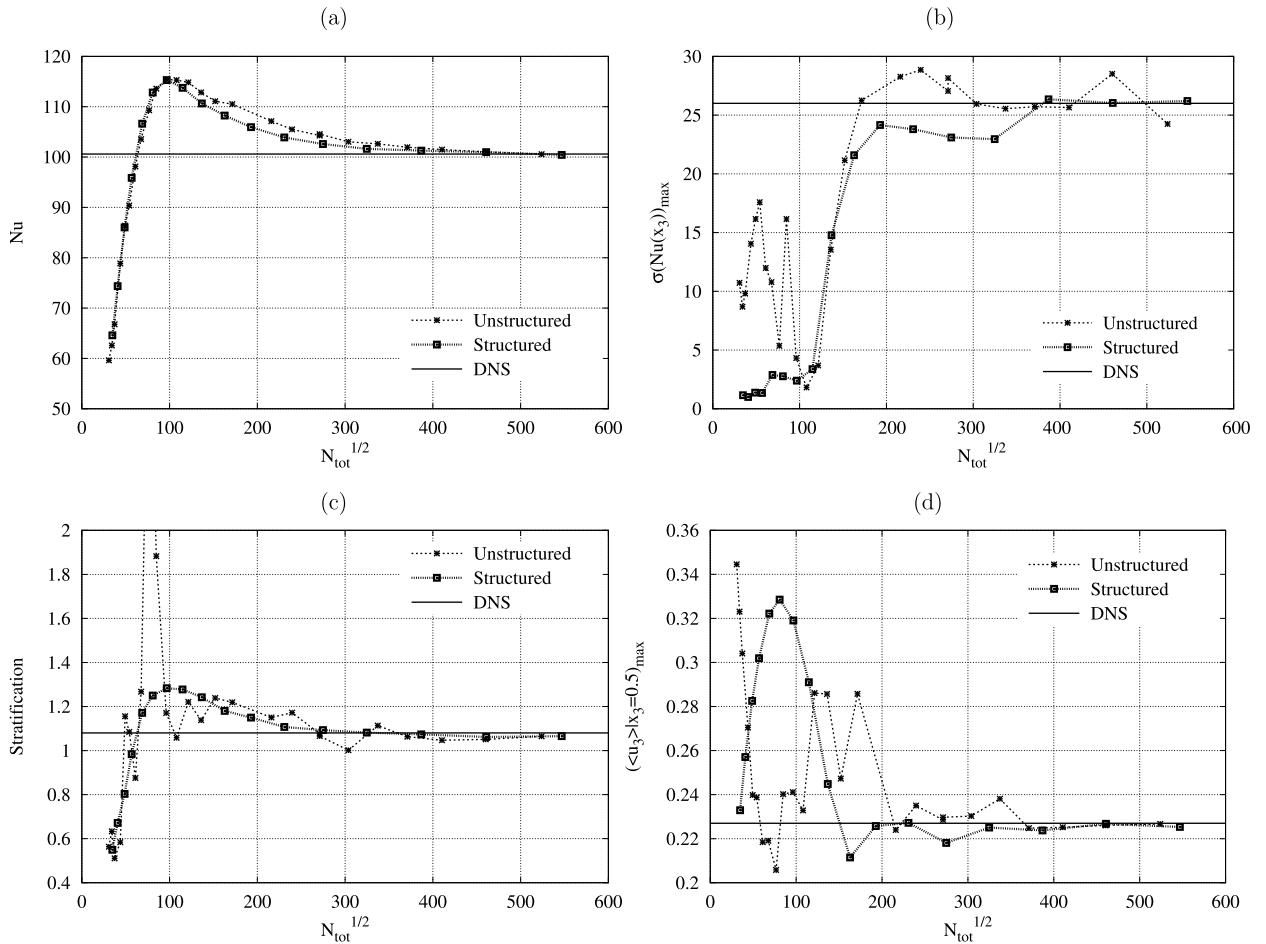
Fig. 10. Convergence study for the collocated formulation on both unstructured and structured grids. (a) Overall averaged Nusselt number, *Nu*. (b) The maximum of the standard deviation of the local Nusselt number. (c) Thermal stratification in the core of the cavity. (d) The maximum $\langle u_3 \rangle$ at the horizontal mid-height plane. The abscissa represents is the root square of the total number of control volumes, N_{tot}.

two finest meshes. For the two coarsest meshes the point of transition clearly moves to upstream positions. This effect can be observed in both the local Nusselt number distribution and the averaged wall-shear stress. This sudden transition increases the top and bottom regions of large fluctuations and, therefore, the area of uniform temperature stratification reduces leading to completely wrong values of the thermal stratification, *C*. As a consequence, for the coarser grids the level of turbulent kinetic energy, $k = \langle \boldsymbol{u}'\boldsymbol{u}' \rangle$, tends to increase at the top and bottom regions of the cavity. Notice that this quantity is only well predicted for the finest MeshA.

5.2. Structured versus unstructured

In this section the performance of the proposed discretization is tested and compared for both structured Cartesian grids and unstructured grids. This kind of comparisons are always difficult because numerical results may be strongly influenced by the quality of the mesh. To minimize these effects, all the meshes have been constructed without any grid refinement. Hence, for the case of structured Cartesian grids, $\gamma_2 = \gamma_3 = 0$ and $N_3 = 4N_2$ whereas the unstructured grids are constructed in the same way than the meshes used to solve the problem given in Eq. (58) (for an illustrative example see Fig. 3, right), except for the fact that now the height aspect ratio is $L_3/L_2 = 4$ instead of 1. Fig. 10 displays a grid convergence study for these two types of meshes. Four different quantities of interest have been analyzed. Namely, the overall Nusselt number, the maximum of the standard deviation of the local Nusselt number, the thermal stratification in the cavity core and the maximum vertical velocity at the horizontal mid-height plane. Notice that the starting point of this analysis corresponds to meshes with a few number of control volumes: $N_{tot} = 1296$ (structured) and $N_{tot} = 948$ (unstructured), respectively. As expected, for these meshes the results are very far from the reference solution. However, as already mentioned above, it is remarkable that since the method is unconditionally stable, numerical results are always obtained even for very coarse meshes. Both the structured and the unstructured simulations convergence to the reference solution. As expected, the simulations carried out on structured grids convergence slightly faster. Of course, this is not the

optimal approach from a computational point-of-view. For instance, MeshA and MeshB have respectively $N_{tot}^{1/2} = \sqrt{89\,240} \approx$ 289.7 and $N_{tot}^{1/2} = \sqrt{44\,988} \approx 212.1$ (see Table 2) and the quality of their solutions is significantly better (for the same mesh size) than the results displayed in Fig. 10. For this particular test-case, the vertical boundary layers must be well resolved to obtain accurate solutions. For the uniform structured meshes, the first grid point is located less than two wall units when $N_{tot}^{1/2} \approx 584$. This approximately corresponds to the finest grid carried out in this convergence analysis. In summary, these results show, not only the robustness of the proposed discretization method, but also its capability to provide accurate numerical solutions for complex turbulent flows for both structured and unstructured grids. Moreover, since the method is unconditionally stable we consider that the proposed symmetry-preserving discretization method forms an excellent starting point for large-eddy simulations in complex geometries.

6. Concluding remarks

The essence of turbulence are the smallest scales of motion. They result from a subtle balance between convective transport and diffusive dissipation. Mathematically, these terms are governed by two differential operators differing in symmetry: the convective operator is skew-symmetric, whereas the diffusive is symmetric and positive-definite. On the other hand, accuracy and stability need to be reconciled for numerical simulations of turbulent flows around complex configurations. With this in mind, a fully-conservative discretization method for general unstructured grids has been developed in the present work. It exactly preserves the symmetries of the underlying differential operators on a collocated mesh. A novel approach to eliminate the checkerboard spurious modes without introducing any non-physical dissipation has also been proposed. It is based on a fully-conservative regularization of the convective term. Therefore, unlike other formulations, the proposed method does not introduce any artificial dissipation which would affect the balance interplayed at the smallest scales. Regarding the accuracy of the method, evidence of the supraconvergence of the discrete Laplacian operator has been numerically showed for a Poisson problem. Finally, the new discretization method has been successfully tested for a turbulent flow in an air-filled differentially heated cavity at Rayleigh number 10^{10}.

In summary, the method is based on only five basic operators: the cell-centered and staggered control volumes, Ω_c and Ω_s, the matrix containing the face normal vectors, N_s, the cell-to-face scalar field interpolation, $\Pi_{c\to s}$ and the divergence operator, M. Once these operators are constructed, the rest follows straightforwardly from them. Therefore, the proposed method constitutes a robust and easy-to-implement approach to solve incompressible turbulent flows in complex configurations. Moreover, we also consider that the symmetry-preserving discretization method presented here forms an excellent starting point for large-eddy simulation. For coarse grids, the energy of the resolved scales of motion is convected in a stable manner: that is, the discrete convective operator transports energy from a resolved scale of motion to other resolved scales without dissipating any energy, as it should do from a physical point-of-view. Therefore, we think that it forms a solid basis for testing sub-grid scale models.

Acknowledgements

Appendix A. Computing and projecting the cell-centered predictor velocity

For staggered velocity fields, the projection onto a divergence-free space is a well-posed problem: given a velocity field, $\boldsymbol{u}_s^p$, it can be uniquely decomposed into a solenoidal vector, $\boldsymbol{u}_s^{n+1}$, and the gradient of a scalar (pressure) field, $\mathsf{G}\tilde{\boldsymbol{p}}_c'$ (see Eq. (14)). This is not the case for collocated velocity fields. The collocated gradient and divergence operators are given by

$$\mathsf{G}_c \equiv -\Omega^{-1}\Gamma_{c\to s}^*\mathsf{M}^* \quad \text{and} \quad \mathsf{M}\Gamma_{c\to s}, \tag{A.1}$$

respectively. These explicit expressions follow straightforwardly from Eqs. (21) and (22). By imposing the incompressibility constraint to $\boldsymbol{u}_c^{n+1}$ ($\mathsf{M}\Gamma_{c\to s}\boldsymbol{u}_c^{n+1} = \mathbf{0}_c$) leads to the following Poisson equation

$$\mathsf{L}_c\,\tilde{\boldsymbol{p}}_c' = \mathsf{M}\Gamma_{c\to s}\boldsymbol{u}_c^p \quad \text{with} \quad \mathsf{L}_c \equiv -\mathsf{M}\Gamma_{c\to s}\Omega^{-1}\Gamma_{c\to s}^*\mathsf{M}^*, \tag{A.2}$$

where the collocated Laplacian operator, $\mathsf{L}_c \in \mathbb{R}^{n\times n}$, is the product of two discrete first-derivative-based symmetric operators. Mathematically, this implies that the kernel has rank higher than 1. Hence, apart from the trivial constant mode, the solution of $\tilde{\boldsymbol{p}}_c'$ may contain non-physical spurious modes. This phenomenon is generally known as checkerboard problem for the pressure (see [25] and references therein, for instance). Hence, one possible solution consists on explicitly removing the components of the pressure field that lie on the kernel of the discrete collocated Laplacian operator, L_c. This is the approach recently proposed by Shashank et al. [25]. However, they tested the method only for structured Cartesian grids where the kernel of L_c is known *a priori*. Although in theory it would be possible, determining this kernel for more complex grids may

eventually become a great numerical challenge. The rest of cures for the checkerboard problem rely on adding (implicitly or explicitly) an interpolated pressure gradient to the face velocity. This eliminates the checkerboard problem for the pressure; however, it introduces a non-physical term to the momentum equation proportional to the third-order derivative of the (pseudo)pressure whose contribution to the kinetic energy does not vanish [31,32]. However, this artificial contribution can be significantly mitigated by an adequate modification of the prediction–correction algorithm. This is briefly analyzed in the following paragraphs.

A.1. What is the right velocity to be computed at the face?

The correction of the cell-centered predictor velocity given in Eq. (27) reads

$$\boldsymbol{u}_c^{n+1} = \left(\mathsf{I} - \Omega^{-1}\mathsf{P}\right)\boldsymbol{u}_c^p, \tag{A.3}$$

where $\mathsf{P} = -\Gamma_{c \to s}^* \mathsf{M}^* \mathsf{L}^{-1} \mathsf{M}\Gamma_{c \to s}$ and the predicted velocity, $\boldsymbol{u}_c^p$, is computed as follows

$$\boldsymbol{u}_c^{p1} = \frac{2\kappa\boldsymbol{u}_c^n - (\kappa - 1/2)\boldsymbol{u}_c^{n-1}}{\kappa + 1/2} + \frac{\Delta t}{\kappa + 1/2}\mathsf{R}\big((1+\kappa)\boldsymbol{u}_c^n - \kappa\boldsymbol{u}_c^{n-1}\big), \tag{A.4}$$

$$\boldsymbol{u}_c^p = \boldsymbol{u}_c^{p1} - \mathsf{G}_c\tilde{\boldsymbol{p}}_c^{\,p}, \tag{A.5}$$

where $\tilde{\boldsymbol{p}}_c^{\,p}$ is a 'prediction' of the pressure at the next time-step, $\tilde{\boldsymbol{p}}_c^{\,n+1} = \tilde{\boldsymbol{p}}_c^{\,p} + \tilde{\boldsymbol{p}}_c^{\,\prime}$. Then, the discrete Poisson equation to be solved results

$$\mathsf{L}\tilde{\boldsymbol{p}}_c^{\,\prime} = \mathsf{M}\boldsymbol{u}_s^p = \mathsf{M}\Gamma_{c \to s}\boldsymbol{u}_c^{p1} - \mathsf{M}\Gamma_{c \to s}\mathsf{G}_c\tilde{\boldsymbol{p}}_c^{\,p}. \tag{A.6}$$

Then, the incompressible velocity field, $\boldsymbol{u}_s^{n+1}$ ($\mathsf{M}\boldsymbol{u}_s^{n+1} = \boldsymbol{0}_c$), results from the following correction step

$$\boldsymbol{u}_s^{n+1} = \boldsymbol{u}_s^p - \mathsf{G}\tilde{\boldsymbol{p}}_c^{\,\prime} = \Gamma_{c \to s}\boldsymbol{u}_c^{p1} - \Gamma_{c \to s}\mathsf{G}_c\tilde{\boldsymbol{p}}_c^{\,p} - \mathsf{G}\tilde{\boldsymbol{p}}_c^{\,\prime}. \tag{A.7}$$

Finally, the cell-centered velocity at the next time-step, $\boldsymbol{u}_c^{n+1}$ results

$$\boldsymbol{u}_c^{n+1} = \boldsymbol{u}_c^{p1} - \mathsf{G}_c\tilde{\boldsymbol{p}}_c^{\,p} - \Omega^{-1}\Gamma_{c \to s}^*\Omega_s\mathsf{G}\tilde{\boldsymbol{p}}_c^{\,\prime} = \boldsymbol{u}_c^{p1} - \mathsf{G}_c\tilde{\boldsymbol{p}}_c^{\,p} - \mathsf{G}_c\tilde{\boldsymbol{p}}_c^{\,\prime}. \tag{A.8}$$

Therefore, the implicit relation between $\boldsymbol{u}_s^{n+1}$ and $\boldsymbol{u}_c^{n+1}$ is given by

$$\boldsymbol{u}_s^{n+1} = \Gamma_{c \to s}\boldsymbol{u}_c^{n+1} + \Gamma_{c \to s}\mathsf{G}_c\tilde{\boldsymbol{p}}_c^{\,\prime} - \mathsf{G}\tilde{\boldsymbol{p}}_c^{\,\prime}, \tag{A.9}$$

and consequently, the error term is given by

$$\boldsymbol{u}_s^{n+1} - \Gamma_{c \to s}\boldsymbol{u}_c^{n+1} = (\Gamma_{c \to s}\mathsf{G}_c - \mathsf{G})\tilde{\boldsymbol{p}}_c^{\,\prime}. \tag{A.10}$$

This has several implications. Firstly, if the convective term is computed using $\boldsymbol{u}_s^{n+1}$, as mentioned above we are introducing an additional term proportional to the third-order derivative of $\tilde{\boldsymbol{p}}_c^{\,\prime}$. Secondly, the cell-centered velocity field $\boldsymbol{u}_c^{n+1}$ is not exactly divergence-free in the sense that

$$\mathsf{M}\Gamma_{c \to s}\boldsymbol{u}_c^{n+1} = -\mathsf{M}(\Gamma_{c \to s}\mathsf{G}_c - \mathsf{G})\tilde{\boldsymbol{p}}_c^{\,\prime} \approx \boldsymbol{0}_c. \tag{A.11}$$

Moreover, the total contribution of the pressure gradient term to the evolution of kinetic energy does not exactly vanish

$$\left(\tilde{\boldsymbol{p}}_c^{\,\prime}\right)^*\mathsf{M}\Gamma_{c \to s}\boldsymbol{u}_c^{n+1} = -\left(\tilde{\boldsymbol{p}}_c^{\,\prime}\right)^*\mathsf{M}(\Gamma_{c \to s}\mathsf{G}_c - \mathsf{G})\tilde{\boldsymbol{p}}_c^{\,\prime}. \tag{A.12}$$

A.1.1. Total pressure (TP) versus pressure correction (PC) approach

Let us briefly analyze the following two approaches: (i) $\tilde{\boldsymbol{p}}_c^{\,p} = \boldsymbol{0}_c$ and (ii) $\tilde{\boldsymbol{p}}_c^{\,p} = \tilde{\boldsymbol{p}}_c^{\,n}$. The former is the classical Chorin projection [34] whereas the later corresponds to the second-order van Kan projection method [42]. Hereafter, they will be referred as total pressure (TP) and pressure correction (PC), respectively. In the first case, the Poisson equation becomes

$$\mathsf{L}\tilde{\boldsymbol{p}}_c^{\,n+1} = \mathsf{M}\Gamma_{c \to s}\boldsymbol{u}_c^{p1}, \tag{A.13}$$

where the pressure at the next time-step in calculated whereas a pressure correction is obtained for the second approach

$$\mathsf{L}\tilde{\boldsymbol{p}}_c^{\,c} = \mathsf{M}\Gamma_{c \to s}\boldsymbol{u}_c^{p1} - \mathsf{M}\Gamma_{c \to s}\mathsf{G}_c\tilde{\boldsymbol{p}}_c^{\,n}. \tag{A.14}$$

The non-physical contribution to the kinetic energy equation given by Eq. (A.12) is actually rather small. Since $\tilde{\boldsymbol{p}}_c^{\,c} = (\tilde{\boldsymbol{p}}_c^{\,n+1} - \tilde{\boldsymbol{p}}_c^{\,n}) \sim \mathcal{O}(\Delta t^2)$ and $\tilde{\boldsymbol{p}}_c^{\,n+1} \sim \mathcal{O}(\Delta t)$, this term scales like $\mathcal{O}(\Delta t^2)$ (TP) and $\mathcal{O}(\Delta t^4)$ (PC), respectively. In this work, in order to minimize this unphysical effect, the pressure correction approach has been adopted. Notice, that in theory, this error can be reduced up to the limit where $\tilde{\boldsymbol{p}}_c^{\,p} = \tilde{\boldsymbol{p}}_c^{\,n+1}$ and $\tilde{\boldsymbol{p}}_c^{\,\prime} = \boldsymbol{0}_c$ and the Poisson equation (A.6) becomes equal to the ill-posed collocated counterpart defined in Eq. (A.2). Apparently, this vicious circle cannot be broken unless we explicitly determine the kernel of the discrete Laplacian operator, L_c.

Appendix B. Origin of the checkerboard spurious modes

We consider that the cell-centered velocity components, $\boldsymbol{u}_c$, can be decomposed into two parts

$$\boldsymbol{u}_c = \boldsymbol{u}_c^\oplus + \boldsymbol{u}_c^\ominus, \tag{B.1}$$

where $\boldsymbol{u}_c^\ominus$, that represents the 'unphysical' components, lies on the kernel of P, $\boldsymbol{u}_c^\ominus \in Ker(\mathsf{P})$. Consequently, these spurious modes cannot be corrected by the pseudo-projection defined in Eq. (27).

Ideally, we would like to retain only the 'physical' realistic modes, $\boldsymbol{u}_c^\oplus$, projecting the vector $\boldsymbol{u}_c$ into the kernel of P. In practice, this is not possible due to its prohibitive costs. Then, the (indirect) strategies to eliminate these spurious modes are twofold: (i) the modification of the pseudo-projector operator to damp the energy contained in these modes and (ii) the non-linear convective term is modified in order to restrain the production of spurious modes. Most of the existing approaches can be grouped into one (or a combination of both) of these strategies. In the following subsections both approaches are briefly analyzed.

B.1. Modifying the pseudo-projection

The total kinetic energy after the pseudo-projection (27) is given by

$$\big\| \boldsymbol{u}_c^{n+1} \big\|^2 = \big((\mathsf{I} - \Omega^{-1}\mathsf{P}) \boldsymbol{u}_c^p \big)^* \Omega \big((\mathsf{I} - \Omega^{-1}\mathsf{P}) \boldsymbol{u}_c^p \big) = \big\| \boldsymbol{u}_c^p \big\|^2 + \big(\boldsymbol{u}_c^p \big)^* \big(\mathsf{P}^*\Omega^{-1}\mathsf{P} - (\mathsf{P} + \mathsf{P}^*) \big) \boldsymbol{u}_c^p. \tag{B.2}$$

Let us consider that the predictor velocity, $\boldsymbol{u}_c^p$, can be split into two parts like in Eq. (B.1). Then the total kinetic energy for the corrected cell-centered velocity, $\boldsymbol{u}_c^{n+1}$, is given by

$$\big\| \boldsymbol{u}_c^{n+1} \big\|^2 = \big\| \boldsymbol{u}_c^p \big\|^2 + \big(\boldsymbol{u}_c^{p,\oplus} + \boldsymbol{u}_c^{p,\ominus} \big)^* \big(\mathsf{P}^*\Omega^{-1}\mathsf{P} - 2\mathsf{P} \big) \big(\boldsymbol{u}_c^{p,\oplus} + \boldsymbol{u}_c^{p,\ominus} \big). \tag{B.3}$$

Since $\boldsymbol{u}_c^\ominus \in Ker(\mathsf{P})$ and matrix P is symmetric, spurious modes would also lie on the kernel of its transpose, $\boldsymbol{u}_c^\ominus \in Ker(\mathsf{P}^*)$. Consequently, previous expression becomes

$$\big\| \boldsymbol{u}_c^{n+1} \big\|^2 = \big\| \boldsymbol{u}_c^p \big\|^2 + \big(\boldsymbol{u}_c^{p,\oplus} \big)^* \big(\mathsf{P}^*\Omega^{-1}\mathsf{P} - 2\mathsf{P} \big) \big(\boldsymbol{u}_c^{p,\oplus} \big). \tag{B.4}$$

Hence, during the pseudo-projection defined in Eq. (27), the energy contained in the spurious modes, $\boldsymbol{u}_c^{p,\ominus}$, is not transferred back to physically realistic modes, $\boldsymbol{u}_c^{p,\oplus}$. The opposite is held only approximately. Moreover, recalling the definition of L_c and P respectively given in Eqs. (A.2) and (27), $\mathsf{P}^*\Omega^{-1}\mathsf{P} = -\Gamma_{c \to s}^* \mathsf{M}^* \mathsf{L}^{-1} (\mathsf{L}_c \mathsf{L}^{-1}) \mathsf{M} \Gamma_{c \to s} \approx -\Gamma_{c \to s}^* \mathsf{M}^* \mathsf{L}^{-1} \mathsf{M} \Gamma_{c \to s} = \mathsf{P}$ and the previous expression can be approximated as

$$\big\| \boldsymbol{u}_c^{n+1} \big\|^2 \approx \big\| \boldsymbol{u}_c^p \big\|^2 - \big(\boldsymbol{u}_c^{p,\oplus} \big)^* \mathsf{P} \big(\boldsymbol{u}_c^{p,\oplus} \big). \tag{B.5}$$

Recalling that P is a positive-definite matrix, we see that pseudo-projection introduces a small damping effect. This is relevant because it guarantees the stability of the method.

On the other hand, if a non-symmetric $\tilde{\mathsf{P}}$ matrix is used instead of P, then some spurious modes may still lie on its kernel but not necessarily on the kernel of its transpose, $\tilde{\mathsf{P}}^* \boldsymbol{u}_c^\ominus \neq \boldsymbol{0}_c$. In this case,

$$\big\| \boldsymbol{u}_c^{n+1} \big\|^2 = \big\| \boldsymbol{u}_c^p \big\|^2 + \big(\boldsymbol{u}_c^{p,\oplus} \big)^* \big(\tilde{\mathsf{P}}^*\Omega^{-1}\tilde{\mathsf{P}} - (\tilde{\mathsf{P}} + \tilde{\mathsf{P}}^*) \big) \big(\boldsymbol{u}_c^{p,\oplus} \big) - 2 \big(\boldsymbol{u}_c^{p,\ominus} \big)^* \tilde{\mathsf{P}} \boldsymbol{u}_c^{p,\oplus}, \tag{B.6}$$

some energy contained in the spurious modes can be transferred back to realistic modes during the velocity field projection. Examples of this kind of approach can be found in [11,57], for instance.

B.2. Stopping the production of spurious modes

Since the diffusive operator, D, is a symmetric positive-definite matrix, it possesses an orthogonal, complete basis of eigenvectors $\boldsymbol{w}_j$

$$\mathsf{D}\boldsymbol{w}_j = \lambda_j \boldsymbol{w}_j, \tag{B.7}$$

where the real-valued eigenvalues are ordered, $0 < \lambda_0 \leqslant \lambda_1 \leqslant \cdots \leqslant \lambda_{3n}$. Thus, we can define the components of $\boldsymbol{u}_c$ with respect to this basis

$$(\tilde{\boldsymbol{u}}_c)_k = \sum_{\lambda_j = k^2} (\hat{\boldsymbol{u}}_c)_j. \tag{B.8}$$

We introduce the notation $\boldsymbol{u}_c^> = \sum_{k>l} (\tilde{\boldsymbol{u}}_c)_k$ and $\boldsymbol{u}_c^< = \sum_{k<l} (\tilde{\boldsymbol{u}}_c)_k$, where l denotes the wavenumber that separates higher and lower (than l) frequency modes, respectively. Then, the evolution of $\|\boldsymbol{u}_c^>\|^2$ and $\|\boldsymbol{u}_c^<\|^2$ can be obtained by left-multiplying Eq. (2a) by $(\boldsymbol{u}_c^>)^*$ and $(\boldsymbol{u}_c^<)^*$, respectively, and summing the resulting expressions with their transpose,

$$\frac{\mathrm{d}}{\mathrm{d}t}\frac{1}{2}\|\boldsymbol{u}_c^>\|^2 = -(\boldsymbol{u}_c^>)^*\mathsf{D}\boldsymbol{u}_c^> - T_l(\boldsymbol{u}_c) + (\boldsymbol{u}_c^>)^*\boldsymbol{f}_c^>, \tag{B.9a}$$

$$\frac{\mathrm{d}}{\mathrm{d}t}\frac{1}{2}\|\boldsymbol{u}_c^<\|^2 = -(\boldsymbol{u}_c^<)^*\mathsf{D}\boldsymbol{u}_c^< + T_l(\boldsymbol{u}_c) + (\boldsymbol{u}_c^<)^*\boldsymbol{f}_c^<, \tag{B.9b}$$

where $T_l(\boldsymbol{u}_c) \equiv (\boldsymbol{u}_c^>)^*\mathsf{C}(\boldsymbol{u}_s)\boldsymbol{u}_c^<$ represents the flux of kinetic energy through the wavenumber l. For simplicity, here the forcing term, $\boldsymbol{f}_c$, includes the rest of terms, *i.e.* body force, pressure gradient, etc. Evolution equations (B.9) resemble the energy budget equations that follow from the incompressible NS equations (1), that is, the non-linear convective term is the responsible to transfer kinetic energy from low- to high-frequencies and vice versa also. This is exactly held in a discrete sense if, and only if, the (skew-)symmetries of the operators are preserved.

On the other hand, the checkerboard spurious modes, $\boldsymbol{u}_c^\ominus$, are associated with the high-frequency modes, $\boldsymbol{u}_c^>$, that lie on the kernel of P operator. Consequently, the convective term is the main responsible of the production of these undesirable modes. Therefore, modifications of the convective term have been proposed [57,58]. However, in doing so, an artificial damping effect is usually introduced.

B.2.1. Effect of the C_4 approximation

In Section 2.4, we have proposed to use the C_4-regularization of the convective operator given in Eq. (34) instead of the C itself. In this case, the energy flux of kinetic energy through the wavenumber l results

$$\widetilde{T_l(\boldsymbol{u}_c)} = T_l(\boldsymbol{u}_c) - ((\boldsymbol{u}_c^>)')^*\mathsf{C}(\boldsymbol{u}_s)(\boldsymbol{u}_c^<)' - ((\boldsymbol{u}_c^>)')^*\mathsf{C}((\boldsymbol{u}_s)')\boldsymbol{u}_c^< - (\boldsymbol{u}_c^>)^*\mathsf{C}((\boldsymbol{u}_s)')(\boldsymbol{u}_c^<)', \tag{B.10}$$

where the prime indicates the residual of the filter, *e.g.* $\boldsymbol{u}_c' = \boldsymbol{u}_c - \overline{\boldsymbol{u}}_c$. If we assume that the filter significantly damps only the high-frequency modes, *i.e.* $\overline{\boldsymbol{u}}_c \approx \boldsymbol{u}_c^<$, then $\widetilde{T_l(\boldsymbol{u}_c)}$ can be approximated by

$$\widetilde{T_l(\boldsymbol{u}_c)} \approx T_l(\boldsymbol{u}_c) - (\boldsymbol{u}_c^>)^*\mathsf{C}(\boldsymbol{u}_s^>)\boldsymbol{u}_c^< = (\boldsymbol{u}_c^>)^*\mathsf{C}(\boldsymbol{u}_s^<)\boldsymbol{u}_c^<. \tag{B.11}$$

In conclusion, the approximation C_4 of the non-linearity results into a smoother convective term; therefore, it prevents the production of checkerboard spurious modes. Moreover, since the discrete convective operator remains skew-symmetric

$$\boldsymbol{w}_c^*\mathsf{C}_4(\boldsymbol{u}_s, \boldsymbol{v}_c) = -\boldsymbol{v}_c^*\mathsf{C}_4(\boldsymbol{u}_s, \boldsymbol{w}_c), \quad \text{if } \mathsf{M}\boldsymbol{u}_s = \boldsymbol{0}_c, \tag{B.12}$$

the C_4-approximation results into an effective way to mitigate the production of checkerboard modes without introducing any non-physical dissipation.

References

[1] U. Frisch, Turbulence. The Legacy of A.N. Kolmogorov, Cambridge University Press, 1995.
[2] R.W.C.P. Verstappen, A.E.P. Veldman, Spectro-consistent discretization of Navier–Stokes: a challenge to RANS and LES, J. Eng. Math. 34 (1998) 163–179.
[3] R.W.C.P. Verstappen, A.E.P. Veldman, Symmetry-preserving discretization of turbulent flow, J. Comput. Phys. 187 (2003) 343–368.
[4] A. Arakawa, Computational design for long-term numerical integration of the equations of fluid motion: two-dimensional incompressible flow, J. Comput. Phys. 1 (1966) 119–143.
[5] A. Arakawa, V.R. Lamb, Computational design of the basic dynamical process of the UCLA general circulation model, Methods Comput. Phys. 17 (1977) 173–265.
[6] Y. Morinishi, T. Lund, O. Vasilyev, P. Moin, Fully conservative higher order finite difference schemes for incompressible flow, J. Comput. Phys. 143 (1998) 90–124.
[7] O.V. Vasilyev, High order finite difference schemes on non-uniform meshes with good conservation properties, J. Comput. Phys. 157 (2000) 746–761.
[8] T.A. Manteuffel, B. Andrew, J. White, The numerical solution of second-order boundary value problems on nonuniform meshes, Math. Comput. 47 (1986) 511–535.
[9] B. Perot, Conservative properties of unstructured staggered mesh schemes, J. Comput. Phys. 159 (2000) 58–89.
[10] X. Zhang, D. Schmidt, B. Perot, Accuracy and conservation properties of a three-dimensional unstructured staggered mesh scheme for fluid dynamics, J. Comput. Phys. 175 (2002) 764–791.
[11] K. Mahesh, G. Constantinescu, P. Moin, A numerical method for large-eddy simulation in complex geometries, J. Comput. Phys. 197 (2004) 215–240.
[12] J.E. Hicken, F.E. Ham, J. Militzer, M. Koksal, A shift transformation for fully conservative methods: turbulence simulation on complex, unstructured grids, J. Comput. Phys. 208 (2005) 704–734.
[13] F. van der Blij, Cell shapes suitable for the shift transformation, Master thesis, Rijksuniversiteit Groningen, The Netherlands, 2007.
[14] J.B. Perot, Discrete conservation properties of unstructured mesh schemes, Annu. Rev. Fluid Mech. 43 (2011) 299–318.
[15] H.B. Keller, A new difference scheme for parabolic problems, in: B. Hubbard (Ed.), Numerical Solutions of Partial Differential Equations II, Academic Press, New York, 1971.
[16] J.B. Perot, V. Subramanian, A discrete calculus analysis of the Keller Box scheme and a generalization of the method to arbitrary meshes, J. Comput. Phys. 226 (1) (2007) 494–508.
[17] M. Shashkov, S. Steinberg, Solving diffusion equations with rough coefficients in rough grids, J. Comput. Phys. 129 (2) (1996) 383–405.
[18] J.M. Hyman, M. Shashkov, Natural discretization for the divergence, gradient, and curl on logically rectangular grids, Comput. Math. Appl. 33 (1997) 81–104.
[19] J.M. Hyman, M. Shashkov, The orthogonal decomposition theorems for mimetic finite difference methods, SIAM J. Numer. Anal. 36 (1999) 788–818.
[20] J.B. Perot, V. Subramanian, Discrete calculus methods for diffusion, J. Comput. Phys. 224 (2007) 59–81.
[21] J. Meyers, B.J. Geurts, P. Sagaut, A computational error-assessment of central finite-volume discretizations in large-eddy simulation using a Smagorinsky model, J. Comput. Phys. 227 (1) (2007) 156–173.
[22] A.E.P. Veldman, K.W. Lam, Symmetry-preserving upwind discretization of convection on non-uniform grids, Appl. Numer. Math. 58 (12) (2008) 1881–1891.

[23] P.K. Subbareddy, G.V. Candler, A fully discrete, kinetic energy consistent finite-volume scheme for compressible flows, J. Comput. Phys. 228 (5) (2009) 1347–1364.
[24] Y. Morinishi, Skew-symmetric form of convective terms and fully conservative finite difference schemes for variable density low-Mach number flows, J. Comput. Phys. 229 (2) (2010) 276–300.
[25] Shashank, J. Larsson, G. Iaccarino, A co-located incompressible Navier–Stokes solver with exact mass, momentum and kinetic energy conservation in the inviscid limit, J. Comput. Phys. 229 (2010) 4425–4430.
[26] M. Chhay, E. Hoarau, A. Hamdouni, P. Sagaut, Comparison of some Lie-symmetry-based integrators, J. Comput. Phys. 230 (5) (2011) 2174–2188.
[27] M. van Reeuwijk, A mimetic mass, momentum and energy conserving discretization for the shallow water equations, Comput. Fluids 46 (1) (2011) 411–416.
[28] B. van't Hof, A.E.P. Veldman, Mass, momentum and energy conserving (MaMEC) discretizations on general grids for the compressible Euler and shallow water equations, J. Comput. Phys. 231 (14) (2012) 4723–4744.
[29] B. Sanderse, Energy-conserving Runge–Kutta methods for the incompressible Navier–Stokes equations, J. Comput. Phys. 233 (1) (2013) 100–131.
[30] F.X. Trias, A. Gorobets, A. Oliva, A simple approach to discretize the viscous term with spatially varying (eddy-)viscosity, J. Comput. Phys. 253 (2013) 405–417.
[31] F. Ham, G. Iaccarino, Energy conservation in collocated discretization schemes on unstructured meshes, Center for Turbulence Research, Annual Research Briefs, 2004, pp. 3–14.
[32] F.N. Felten, T.S. Lund, Kinetic energy conservation issues associated with the collocated mesh scheme for incompressible flow, J. Comput. Phys. 215 (2006) 465–484.
[33] F.X. Trias, O. Lehmkuhl, A self-adaptive strategy for the time-integration of Navier–Stokes equations, Numer. Heat Transf., Part B, Fundam. 60 (2) (2011) 116–134.
[34] A.J. Chorin, Numerical solution of the Navier–Stokes equations, J. Comput. Phys. 22 (1968) 745–762.
[35] N.N. Yanenko, The Method of Fractional Steps, Springer-Verlag, 1971.
[36] J.B. Perot, An analysis of the fractional step method, J. Comput. Phys. 108 (1993) 51–58.
[37] A.J. Chorin, J.E. Marsden, A Mathematical Introduction to Fluid Mechanics, 3rd edition, Springer, 2000.
[38] R. Borrell, O. Lehmkuhl, F.X. Trias, A. Oliva, Parallel direct Poisson solver for discretizations with one Fourier diagonalizable direction, J. Comput. Phys. 230 (2011) 4723–4741.
[39] C.M. Rhie, W.L. Chow, Numerical study of the turbulent flow past an airfoil with trailing edge separation, AIAA J. 21 (1983) 1525–1532.
[40] S. Armfield, R. Street, A comparison of staggered and non-staggered grid Navier–Stokes solutions for the 8:1 cavity natural convection flow, ANZIAM J. 46 (2004) C918–C934.
[41] S.W. Armfield, N. Williamson, M.P. Kirkpatrick, R. Street, A divergence free fractional-step method for the Navier–Stokes equations on non-staggered grids, ANZIAM J. 51 (2009) C654–C667.
[42] J. van Kan, A second-order accurate pressure-correction scheme for viscous incompressible flows, SIAM J. Sci. Stat. Comput. 7 (1986) 870–891.
[43] J.L. Guermond, J.T. Oden, S. Prudhomme, Mathematical perspectives on large eddy simulation models for turbulent flows, J. Math. Fluid Mech. 6 (2004) 194–248.
[44] B.J. Geurts, D.D. Holm, Regularization modeling for large-eddy simulation, Phys. Fluids 15 (2003) L13–L16.
[45] J. Leray, Sur le movement d'un liquide visqueaux emplissant l'espace, Acta Math. 63 (1934) 193–248.
[46] A. Cheskidov, D.D. Holm, E. Olson, E.S. Titi, On a Leray-α model of turbulence, Proc. R. Soc. A, Math. Phys. Eng. Sci. 461 (2055) (2005) 629–649.
[47] B.J. Geurts, D.D. Holm, Leray and LANS-α modelling of turbulent mixing, J. Turbul. 7 (2006) 1–33.
[48] M. van Reeuwijk, H.J.J. Jonker, K. Hanjalić, Leray-α simulations of wall-bounded turbulent flows, Int. J. Heat Fluid Flow 30 (6) (2009) 1044–1053.
[49] R. Verstappen, On restraining the production of small scales of motion in a turbulent channel flow, Comput. Fluids 37 (2008) 887–897.
[50] D. Carati, G.S. Winckelmans, H. Jeanmart, Exact expansions for filtered-scales modelling with a wide class of LES filters, in: Direct and Large-Eddy Simulation III, Kluwer, 1999, pp. 213–224.
[51] P. Sagaut, R. Grohens, Discrete filters for large eddy simulations, Int. J. Numer. Methods Fluids 31 (1999) 1195–1220.
[52] F.X. Trias, R.W.C.P. Verstappen, On the construction of discrete filters for symmetry-preserving regularization models, Comput. Fluids 40 (2011) 139–148.
[53] S. Barbeiro, Supraconvergent cell-centered scheme for two-dimensional elliptic problems, Appl. Numer. Math. 59 (2009) 56–72.
[54] A.E.P. Veldman, K. Rinzema, Playing with nonuniform grids, J. Eng. Math. 26 (1992) 119–130.
[55] D.G. Barhaghi, L. Davidson, Natural convection boundary layer in a 5:1 cavity, Phys. Fluids 19 (12) (2007) 125106.
[56] F.X. Trias, M. Soria, A. Oliva, C.D. Pérez-Segarra, Direct numerical simulations of two- and three-dimensional turbulent natural convection flows in a differentially heated cavity of aspect ratio 4, J. Fluid Mech. 586 (2007) 259–293.
[57] L. Davidson, A pressure correction method for unstructured meshes with arbitrary control volumes, Int. J. Numer. Methods Fluids 22 (1996) 265–281.
[58] S. Nägele, G. Wittum, On the influence of different stabilisation methods for the incompressible Navier–Stokes equations, J. Comput. Phys. 224 (2007) 100–116.